

# Coupled modeling of thermics and hydrogeology with the Cast3M code: application to the Rainbow hydrothermal field (Mid-Atlantic Ridge, 36°14'N)

Florian Perez · Claude Mügler ·  
Philippe Jean-Baptiste · Jean Luc Charlou

Received: 13 January 2012 / Accepted: 9 October 2012  
© Springer Science+Business Media Dordrecht 2012

**Abstract** We present a new numerical tool developed in the Cast3M software framework to model hydrothermal circulation. Thermodynamic properties of one-phase pure water are calculated from the International Association for the Properties of Water and Steam formulation. This new numerical tool is validated on several test cases of convection in closed-top and open-top boxes. Simulations of hydrothermal circulation in a homogeneous-permeability porous medium also give results in good agreement with already published simulations. This new numerical tool is used to construct a geometric and physical conceptual model of the Rainbow vent site at 36°14'N on the Mid-Atlantic Ridge. Several configurations are discussed, showing that high temperatures and high mass fluxes measured at the Rainbow site cannot be modeled with hydrothermal circulation in a homogeneous-permeability porous medium. These high values require the presence of a fault or a preferential pathway right below the venting site. We propose and discuss a two-dimensional single-pass model that allows us to simulate both high temperatures and high mass fluxes. This modeling of the hydrothermal circulation at the Rainbow site constitutes the first but necessary step to understand the origin of high concentrations of hydrogen issued from this ultramafic-hosted vent field.

**Keywords** Hydrothermal system · Mid-ocean ridge · Numerical modeling · Rainbow vent site · Permeability

## 1 Introduction

Hydrothermal activity at the axis of mid-ocean ridges is a key driver of energy and matter transfer from the interior of the Earth to the ocean floor. At mid-ocean ridges, seawater penetrates through the permeable young crust, warms at depth, and exchanges chemicals with the surrounding rocks. This hot fluid focuses and flows upwards and is then expelled from the crust at hydrothermal vent sites in the form of black or white smokers completed by diffusive emissions [15, 59, 66]. These heat-driven fluid flows are conditioned by multiple complex phenomena. According to the studied fields, chemical and physical clues can reveal, more or less clearly, the existence of phase separation [6–9, 28, 71], thermal and seismic fracturing, and retroactions of geochemical reactions such as microfractures or heat production [49, 60, 64].

In the last few decades, numerical modeling of mid-ocean ridge hydrothermal systems has been very helpful to partly explain the role of some phenomena, such as phase separation [19, 29, 41, 46]. Modeling of such complex systems requires high computational power. Thus, even quite recently, most of the studies about heat-driven fluids in porous media used the Boussinesq approximation [14, 37, 62]. In the Boussinesq approximation, all density variations are neglected except for the buoyancy term in the equation of motion. Most of the authors also assumed a linear dependence of fluid density with temperature and a constant fluid

F. Perez (✉) · C. Mügler · P. Jean-Baptiste  
Laboratoire des Sciences du Climat et de l'Environnement,  
CEA-CNRS-UVSQ, Orme des Merisiers,  
91191 Gif-sur-Yvette, France  
e-mail: florian.perez@lscce.ipsl.fr

F. Perez · J. L. Charlou  
Département Géosciences Marines, Centre de Brest,  
IFREMER, Plouzané, France

viscosity [4, 14, 37]. The main advantage of these approximations is to drastically reduce the degree of coupling between the partial differential equations and, therefore, to lower the computing time. However, it was shown that the linearized properties tend to stabilize the convection [67] and that the use of the Boussinesq approximation leads to underestimated water and heat fluxes [72] and to overestimated surface discharge of the system [16].

Recently, more complex codes have been developed using realistic pure-water properties [16, 18] or seawater properties [19, 24–26, 29, 30, 45]. Most of these codes are able to model multiphase flows and phase separation [19, 29, 30, 45, 46]. Other codes take the averaged properties of the hydrothermal fluid [24]. All these codes reproduced the high temperatures of exiting fluids from black-smoker hydrothermal sites. However, although the two-dimensional (2D) modeling leads to simulated heat and mass fluxes, which are in agreement with large space-scale estimate at about 100 MW/km of ridge [26, 46], a few models focused on a description of single-site fluxes. After the three-dimensional (3D) modeling of Travis et al. [69] who used linear properties and of Rabinowicz et al. [57, 58] who used the equations of state for seawater derived by Potter and Brown [56], Coumou et al. [17, 18] simulated a 3D hydrothermal circulation along the ridge axis using pure-water properties and showed that fluid flow converges in water columns which are regularly arrayed along the ridge axis. For a permeability  $k = 10^{-13} \text{ m}^2$ , they calculated water mass fluxes at the discharge zone on the order of  $10^{-3} \text{ kg s}^{-1} \text{ m}^{-2}$ , which is about ten times lower than the estimated fluxes of hydrothermal sites such as the Rainbow vent site [3, 33, 38].

Based on these previous studies, we developed a new numerical tool to model hydrothermal circulation in the perspective of geochemical applications.

The present paper describes the modeling tool that we developed in the Cast3M framework, its validation, and one application. Cast3M is a numerical simulation program that was first developed at the Commissariat à l'Énergie Atomique et aux Énergies Alternatives in France for structural mechanics and thermohydraulics (<http://www-cast3m.cea.fr>). The starting point of this code considers that a given partial differential equation (PDE)-type problem can be solved by a sequence of elementary operators [53]. As a consequence, Cast3M, a free code for research and teaching that consists of a collection of more than 500 such operators, can be seen as a powerful toolbox to solve problems in many domains including mechanics, thermics, and hydraulics.

The first purpose of our paper is to present the use of Cast3M to the coupling of the heat transport equation

with fluid mass transport equations in a hydrogeological context. This new numerical tool and its validation are presented in Sections 2 and 3, respectively. Section 4 is devoted to the application of the code to modeling hydrothermal water circulation at mid-ocean ridges. We chose the Rainbow vent site which is located on the Mid-Atlantic Ridge at  $36^{\circ}13.8'N-33^{\circ}54.15'W$ , at a depth of about 2,300 m. The first measurements of this site were taken in 1994 during the HEAT cruise-CD89 [32]. This site has since been explored and described several times [11, 12, 20, 63]. One of the most interesting chemical characteristics of the fluids emitted by the ten active chimneys of the Rainbow vent site is very high hydrogen concentrations. However, the origin of such high concentrations is still under discussion [12, 51, 63]. To understand and model the production of hydrogen, it is first necessary to have a baseline knowledge of the hydraulic characteristics of the site. In the last part of this paper, using a conceptual model of the Rainbow vent site, we investigate first-order consequences of the geometrical and physical configurations on the simulated fluxes and temperatures of the exiting fluids. Finally, the hydrogeological context of the Rainbow hydrothermal circulation is studied not only because of its unique chemical characteristics but also because of its available reported data, such as estimated mass fluxes [33, 39], measured temperatures [12, 20, 63], and, while debatable, the depth at which phase separation occurs at the Rainbow site [12], all of which are constraints for the conceptual modeling we present here (see Section 4.4).

## 2 Methods

### 2.1 Governing equations

The model we used in this study is based on equations of fluid mass and energy balance. The important parameters and unknowns are given in Table 1. Since the velocity of water through porous media is “of low value,” it is usually described by Darcy’s law:

$$\vec{v} = -\frac{k}{\mu_f} \left( \vec{\nabla} P - \rho_f \vec{g} \right). \quad (1)$$

By doing mass balance on an infinitely small volume, we can write the commonly used mass balance equation:

$$\frac{\partial \phi \rho_f}{\partial t} + \vec{\nabla} \cdot \rho_f \vec{v} = 0. \quad (2)$$

If we assume that the compressibility of water is orders of magnitude greater than that of rock and consider

**Table 1** Unknowns and physical parameters

Symbol	Quantity	Unit
$\alpha_f$	Fluid expansivity	$^{\circ}\text{C}^{-1}$
$\beta_f$	Fluid compressibility	$\text{Pa}^{-1}$
$\lambda_{\text{eff}}$	Thermal conductivity	$\text{J m}^{-1} \text{s}^{-1} ^{\circ}\text{C}^{-1}$
$\mu_f$	Fluid dynamic viscosity	$\text{Pa s}$
$\rho_f$	Fluid density	$\text{kg m}^{-3}$
$\rho_r$	Rock density	$\text{kg m}^{-3}$
$c_f$	Fluid isobaric heat capacity	$\text{J kg}^{-1} ^{\circ}\text{C}^{-1}$
$c_r$	Rock isobaric heat capacity	$\text{J kg}^{-1} ^{\circ}\text{C}^{-1}$
$\phi$	Porosity	–
$g$	Gravitational acceleration	$\text{m s}^{-2}$
$P$	Pressure	$\text{Pa}$
$T$	Temperature	$^{\circ}\text{C}$
$\vec{v}$	Darcy velocity	$\text{m s}^{-1}$
$k$	Intrinsic permeability	$\text{m}^2$

that  $\rho_f$  is only a function of temperature  $T$  and pressure  $P$ , we obtain the basic mass balance equation:

$$\phi \rho_f \beta_f \frac{\partial P}{\partial t} = \vec{\nabla} \cdot \left( \frac{\rho_f k}{\mu_f} \vec{\nabla} P \right) - \vec{\nabla} \cdot \left( \frac{\rho_f^2 k}{\mu_f} \vec{g} \right) + \phi \rho_f \alpha_f \frac{\partial T}{\partial t}, \tag{3}$$

where  $\alpha_f$  and  $\beta_f$  are the thermal expansivity and compressibility of the fluid, respectively:

$$\alpha_f = - \frac{1}{\rho_f} \frac{\partial \rho_f}{\partial T} \Big|_P, \tag{4}$$

$$\beta_f = \frac{1}{\rho_f} \frac{\partial \rho_f}{\partial P} \Big|_T. \tag{5}$$

Since we assume local equilibrium between rock and water, the energy balance equation can be written as

$$(\phi \rho_f c_f + (1 - \phi) \rho_r c_r) \frac{\partial T}{\partial t} = \vec{\nabla} \cdot (\lambda_{\text{eff}} \vec{\nabla} T - \rho_f c_f \vec{v} T). \tag{6}$$

This formulation forces water to completely share the heat transported with rock. Thus, this formulation can, in a way, favor heat diffusion. Finally, the system to be solved is composed of the two spatial- and time-dependent coupled Eqs. 3 and 6.

### 2.2 Fluid properties

In mid-ocean ridge hydrothermal systems, water temperature and pressure can eventually vary from 2 to about 1,200 °C and from 10 to more than 500 bars, respectively. Consequently, the dependence on  $P$  and  $T$  of the thermodynamic properties of water such as density, thermal expansivity, compressibility, specific heat, and viscosity must be taken into account. We

used the International Association for the Properties of Water and Steam (IAPWS) formulation for the pure-water properties [35]. A polynomial formulation of the equations of state for seawater was also implemented [68]. Only single-phase flows are taken into account: involved fluids are pure water in supercritical state or pure water or seawater at lower temperatures and high pressure.

### 2.3 Numerical methods

Both Eqs. 3 and 6 can be written as the following transport equation:

$$\phi \frac{\partial C}{\partial t} = \vec{\nabla} \cdot (D \vec{\nabla} C - \vec{v} C) + S, \tag{7}$$

where the transported quantity  $C$  is the pressure  $P$  for the mass balance Eq. 3 and the temperature  $T$  for the energy balance Eq. 6. The generic transport Eq. 7 is solved in the framework of the Cast3M code (<http://www-cast3m.cea.fr>). We used a first-order implicit time scheme and a finite-volume method for spatial discretization with the BiCGSTAB solver [5]. BiCGSTAB is a biconjugate gradient stabilized algorithm for solving nonsymmetric systems [70]. This scheme was used with incomplete Crouté lower-upper decomposition as a preconditioner. The diffusive part of Eq. 7 is solved with a finite-volume method using the multipoint flux approximation described in [1]. This scheme is conservative, and numerical evidence shows a second-order accuracy in the L2 norm [31, 44]. For the convective part, the spatial scheme depends on the value of the Peclet number  $Pe$  [44]: the scheme degenerates into a second-order accuracy centered scheme for dominant diffusion transport ( $Pe < 2$ ) and into a first-order upwind scheme for dominant advective transport. Regardless of the Peclet number, this scheme remains stable on regular grids [44]. Here, the Peclet number, denoted  $Pe$ , is a dimensionless number calculated in each cell of the mesh as  $Pe = (|\vec{v}| \ell / D)$ , where  $\ell$  is the characteristic length of the cell,  $|\vec{v}|$  is the norm of the fluid velocity in the cell, and  $D$  is the diffusion coefficient defined in Eq. 7. The numerical scheme must be able to solve highly nonlinear coupled equations both at long and short time scales (from a few days to thousands of years) and spatial scales (from a few meters to several kilometers). Indeed, phenomena occurring over a few days or months, such as the birth of plumes in the established main circulation, and over a few meters scale, such as boundary layer destabilization or plume splitting, can have significant consequences on the overall behavior of the hydrothermal systems. Thus, we implemented two different algorithms to solve the coupled PDEs

(3–6). The first one is a simple sequential algorithm, which requires small time steps of calculation to be stable and accurate. In the second algorithm, the two PDEs (3–6) are linearized with a Picard’s scheme and solved iteratively. The Picard’s method is an iterative method for solving nonlinear equations [36]. It is a commonly used procedure for solving the nonlinear equation governing flow in variably saturated porous media [43, 55]. The general algorithm for Picard iteration can be described as follows. Consider a nonlinear equations written in the form

$$A \frac{\partial c}{\partial t} + Bc = S, \tag{8}$$

where  $A$  and  $B$  are matrices that depend on the unknown  $c$  and  $S$  is a vector. The standard Picard scheme is given by

$$\left( \frac{A^{n+1,k}}{\Delta t^{n+1}} + B^{n+1,k} \right) c^{n+1,k+1} = S^{n+1,k} + \left( \frac{A^{n+1,k}}{\Delta t^{n+1}} \right) c^n, \tag{9}$$

where  $k$  denotes the iteration number such that  $c^{n+1,0} = c^n$  is the initial estimate, and where  $n$  is the time step. In Eq. 9, the left-side matrix and the right side are updated at each iterative cycle. The iteration is performed until satisfactory convergence is achieved. A typical criterion for checking convergence is given by

$$\frac{\max |c^{n+1,k+1} - c^{n+1,k}|}{\max |c^{n+1,k+1}|} \leq \epsilon, \tag{10}$$

where  $\epsilon$  is a prescribed tolerance for the  $c$  value. In our case, we used the Picard’s method with  $\epsilon = 10^{-3}$ . We always started our calculations with the Picard’s iterative scheme because of its accuracy and stability. When it was possible, we switched the Picard’s algorithm to the sequential algorithm to reduce computing time. In both algorithms, we first solve the energy balance equation and then the mass balance equation. Both sequential and iterative schemes have been tested in all the configurations presented in the following sections. They always led to very close results.

### 3 Numerical experiments

#### 3.1 Experiments with the Boussinesq approximation

We first applied the numerical code to standard configurations using the Boussinesq approximation and linear dependence of density on temperature to compare numerical solutions with results already published.

In the Boussinesq approximation, all density variations are neglected except for the gravity term in Darcy’s law. The fluid mass balance Eq. 2 reduces to the formulation for incompressible fluids

$$\vec{\nabla} \cdot \vec{v} = 0. \tag{11}$$

The fluid density is approximated by a linear function of temperature

$$\rho_f(T) = \rho_f(T_{\max}) \times [1 - \alpha_f(T - T_{\max})], \tag{12}$$

where  $\alpha_f$  is the constant thermal expansivity of the fluid. In this section, we assume that the two terms  $\rho_f c_f$  and  $\rho_r c_r$  are equal and constant. Hence, the energy balance Eq. 6 reduces to

$$\frac{\partial T}{\partial t} = \vec{\nabla} \cdot (\kappa_{\text{therm}} \vec{\nabla} T - \vec{v} T), \tag{13}$$

where  $\kappa_{\text{therm}}$  represents the thermal diffusivity of the saturated porous medium.

In the following, we note  $T_{\max}$  and  $T_{\min}$  the maximum and minimum temperatures, and  $\rho_{\min}$  and  $\rho_{\max}$  the corresponding densities given by Eq. 12. The problem is non-dimensionalized with the specific dimension  $L$  of the domain as the length scale, the temperature difference  $\Delta T = (T_{\max} - T_{\min})$  as the temperature scale, the thermal conduction time  $L^2/\kappa_{\text{therm}}$  as the time scale, the difference  $\Delta \rho = (\rho_{\max} - \rho_{\min})$  as the density scale,  $(k/\mu_f)\Delta \rho g$  as the velocity scale, and  $\Delta \rho g L$  as the pressure scale. The dimensionless equations are the following:

- For the Darcy velocity,

$$\vec{v}^* = - \left( \vec{\nabla}^* P^* + \rho_f^* \vec{e}_z \right), \tag{14}$$

- For the mass balance equation,

$$\vec{\nabla}^* \cdot \vec{v}^* = 0, \tag{15}$$

- For the energy balance equation,

$$\frac{\partial T^*}{\partial t^*} + \text{Ra} \times (\vec{v}^* \cdot \vec{\nabla}^* T^*) = \vec{\nabla}^* \cdot (\vec{\nabla}^* T^*), \tag{16}$$

- For the fluid density,

$$\rho_f^*(T^*) = \rho_f^*(T_{\max}^*) \times [1 - \alpha_f \Delta T (T^* - T_{\max}^*)]. \tag{17}$$

Here, the asterisk  $*$  means non-dimensionalized quantities,  $\vec{e}_z$  is the unit vector pointing upward, and the Rayleigh number  $\text{Ra}$  is a dimensionless parameter defined as

$$\text{Ra} = \frac{\Delta \rho g L k}{\mu_f \kappa_{\text{therm}}}. \tag{18}$$

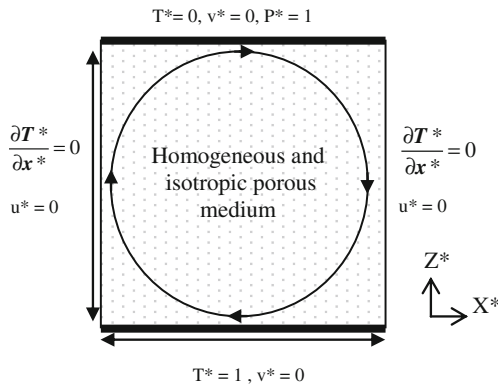


**Fig. 1** Model setup for the convection in a closed-top system. Constant temperature and zero velocities are imposed both at the top and the bottom of the domain ( $u^*$  and  $v^*$  are the horizontal and vertical components of the dimensionless Darcy velocity, respectively)

This non-dimensional parameter determines the flow patterns and the temperature field. In addition to the Rayleigh number, it is useful to introduce another global measure of convective vigor, the Nusselt number  $Nu$ . For a layer heated from below, the Nusselt number can be defined as

$$Nu = - \int_0^1 \frac{\partial T^*}{\partial z^*} \Big|_{z^*=0} dx^* \tag{19}$$

The Nusselt number provides a dimensionless measure of the heat flux and corresponds to the ratio of the observed conductive heat flux to that in the absence of convection. Since  $Nu = 1$  when there is no convection,  $(Nu - 1)$  is the dimensionless convective heat flux.

### 3.1.1 Convection in a closed-top system

In order to benchmark our numerical model, we first simulated convection in a closed box and compared our

results with previously published data [10, 14, 24]. Convection is confined in a two-dimensional box of length  $L = 1$  and is driven by a vertical temperature difference  $\Delta T$ . The top and bottom boundaries are isothermal and impermeable. The side boundaries are axes of symmetry (see Fig. 1). Calculations are performed with a two-dimensional mesh of  $96 \times 96$  cells and  $128 \times 128$  cells. We verified that spatial convergence was reached with such spatial resolutions. In all calculations, the maximum value of the Peclet number was lower than 2. As a consequence, the scheme is second-order accurate in space.

We performed simulations for three values of the Rayleigh number:  $Ra = 800$ ,  $Ra = 950$ , and  $Ra = 1,200$ . For  $Ra = 800$ , the initial temperature field was a vertical diffuse field with a constant temperature gradient. The temperature field obtained at the end of the simulation performed at  $Ra = 800$  was then used as initial condition for the calculations at  $Ra = 950$  and  $Ra = 1,200$  (Fig. 2). For these large  $Ra$  numbers, the simulated system is unsteady as the Nusselt number calculated at the bottom boundary oscillates with time (Fig. 3). As seen in Table 2, the time-averaged Nusselt numbers and oscillation frequencies calculated from Cast3M simulations are in good agreement with previously published studies [10, 14, 24, 34].

### 3.1.2 Convection in an open-top system

The second step was to simulate convection in an open-top 2D box. The bottom boundary is isothermal and impermeable; the side boundaries are axes of symmetry (Fig. 4). At the top boundary, the temperature of the fluid which penetrates the permeable medium is fixed at  $T^* = 0$  although a zero heat flux condition is imposed for the fluid exiting the medium. Calculations

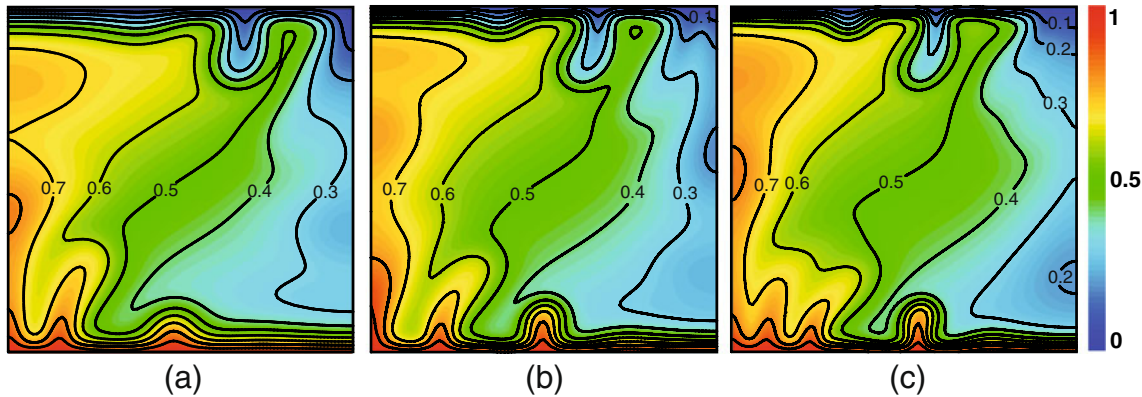


**Fig. 2** Convection in a closed-top system. Temperature fields obtained at a non-dimensionalized time greater than 1, for various Rayleigh numbers: **a**  $Ra = 800$ , **b**  $Ra = 950$ , and **c**  $Ra = 1,200$

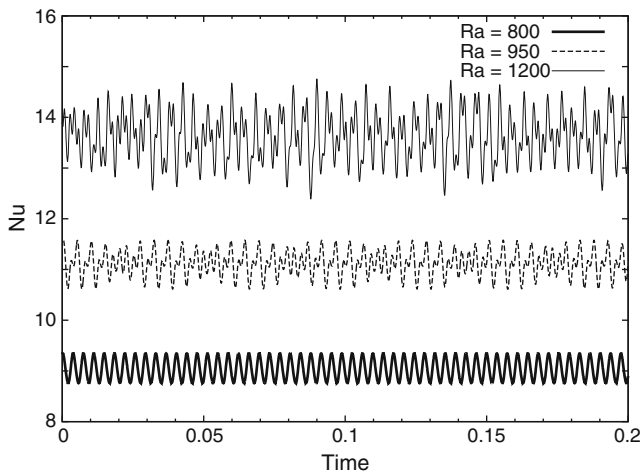


**Fig. 3** Convection in a closed-top system. Time evolution of the Nusselt number for various Rayleigh numbers: Ra = 800, Ra = 950, and Ra = 1,200. A Fourier transformation leads to a unique oscillatory frequency  $f_1=283$  for Ra = 800, to two frequencies,  $f_1=399$  and  $f_2=212$ , for Ra = 950, and  $f_1=595$  and  $f_2=230$  for Ra = 1,200 (see Table 2)

are performed with the same mesh as the one used in Section 3.1.1.

We performed several simulations for Rayleigh numbers in the range 30 to 425 as well as 500 and 1,000. Figure 5 displays the evolution of steady-state Nusselt numbers as a function of the Ra number. It clearly

**Table 2** Convection in a closed-top system

Ra	800	950	1,200	Reference
Nu <sub>seq</sub>	9.1	10.9	13.6	This study, sequential algorithm
$f_1$	280	399	595	
$f_2$		212	230	
Nu <sub>ite</sub>	9.12	10.9	13.6	This study, iterative algorithm
$f_1$	283	399	595	
$f_2$		212	230	
Nu	9.2	10.9	13.06	[24]
$f_1$	275	397	608	
$f_2$		200	228	
Nu	9.14			[14]
$f_1$	299			
$f_2$				
Nu	9.43		13.85	[10]
$f_1$			695	
$f_2$			261	
$f_3$			69	

Comparison of numerical results for three various Rayleigh numbers: Ra = 800, Ra = 950, and Ra = 1,200. Nusselt numbers Nu are averaged over a characteristic timescale and frequencies  $f_i$  are calculated from Fourier transformations. Nu<sub>seq</sub> and Nu<sub>ite</sub> denote the Cast3M results obtained with the sequential and iterative algorithms, respectively

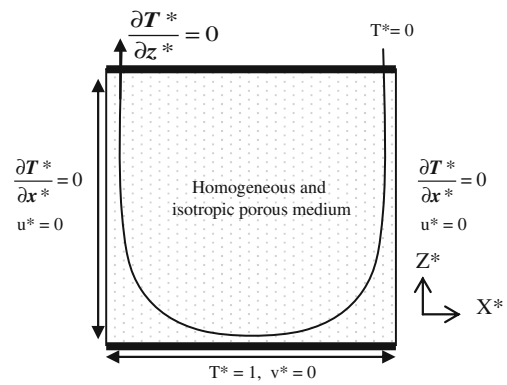


**Fig. 4** Model setup for the convection in an open-top system. Fluid at  $T^* = 0$  penetrates into the permeable medium and exits with a diffusive heat flux equal to zero

shows that the calculated Nusselt numbers obtained from Cast3M simulations are in good agreement with previously published results [14, 22, 24]. Figure 6a, b displays the evolution of the Nusselt number and the associated frequency spectra with time for a chaotic regime (Ra = 500) and a periodic regime (Ra = 1,000). For Ra = 500, the chaotic regime we simulated exhibits an evolution of the Nusselt number versus time which is similar to the one published by Cherkaoui and Wilcock [14]. The maximum of the Nusselt number reaches 14.7. Its minimum is 9.8 which corresponds to the linear horizontal part of the evolution. For Ra = 1,000, we found one fundamental oscillation frequency equal to 481, very close to the  $514 \pm 5$  of Cherkaoui and Wilcock [14] and to the 490 of Fontaine and Wilcock [24]. The minimum value of the Nusselt number is equal to 17.8 and its amplitude to 1.05.

The Cast3M results for both open- and closed-top systems are in good agreement with the literature. These results confirm the stability and accuracy of our code and allow us to validate our numerical code in the case of the Boussinesq approximation.

### 3.2 Experiments with fluid properties function of $T$ and $P$

Wilcock [72] and Coumou et al. [16] have shown that when taking into account the dependence of water properties on temperature and pressure, convection is much more vigorous than when the Boussinesq approximation is used. For a 1,000-m-deep domain with a bottom boundary condition  $T = 1,000$  °C and a low intrinsic permeability, Coumou et al. [16] showed that the surface area through which hot fluids exit is four times larger in simulations based on the Boussinesq approximation than in simulations in which the full Eqs. 3 and 6

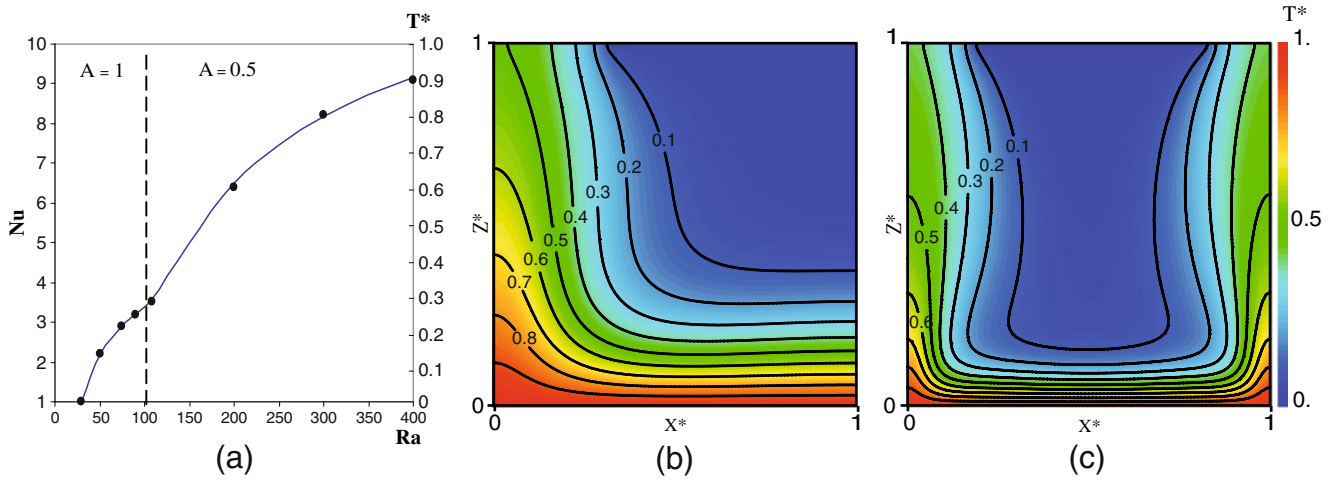


**Fig. 5** Convection in an open-top system. **a** Steady-state Nusselt number  $Nu$  as a function of Rayleigh number  $Ra$  for a constant temperature top boundary. The *solid line* represents an interpolation from 15 simulations performed with Cast3M. *Filled circles* indicate previously published data [14]. The  $A$  value corresponds to the aspect ratio of the convective cells (width/height). **b** and **c** are steady temperature field obtained for  $Ra = 90$  and  $Ra = 300$ , respectively

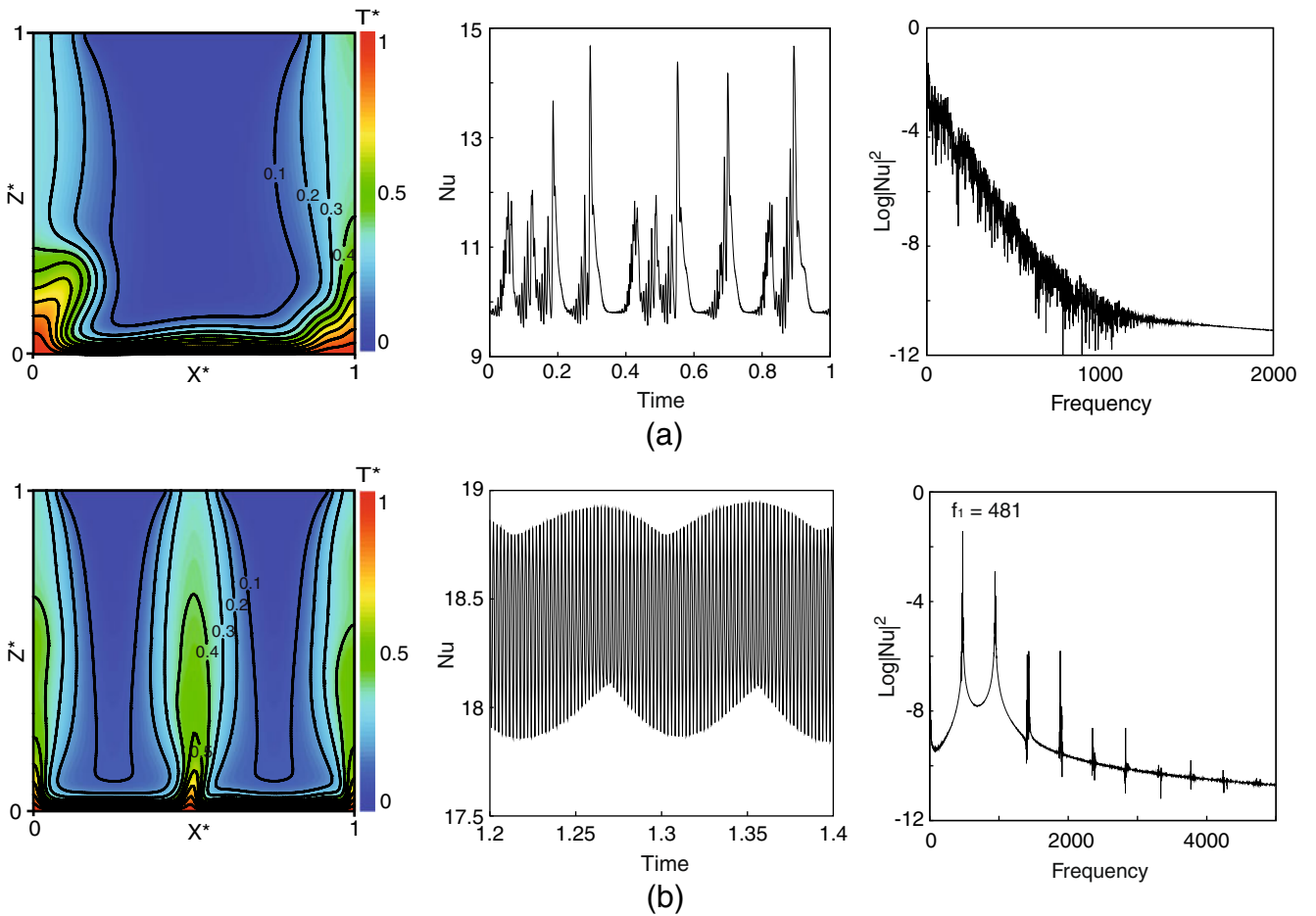


**Fig. 6** Convection in an open-top system. Unsteady temperature fields (*solid lines* indicate isotherms), evolution of Nusselt number versus time, and frequency spectra from simulations for **a**  $Ra = 500$  and **b**  $Ra = 1,000$

and full equations of state (EOS) are solved together. In this subsection, we test the solving of the complete system of equations with full varying properties of pure water with temperature and pressure according to IAPWS formulation [35]. At low permeability values ( $k = 10^{-15} \text{ m}^2$ ), the simulations performed by Coumou et al. [16] exhibit a steady-state convection with exiting fluid temperature about  $385 \text{ }^\circ\text{C}$ . With a greater permeability ( $10^{-14}$  up to  $10^{-13} \text{ m}^2$ ), convection becomes unstable and fluid exits at about  $375 \pm 20 \text{ }^\circ\text{C}$ . Fontaine and Wilcock [24] used a model setup that is closer to the one used here for validations. They imposed a temperature of  $600 \text{ }^\circ\text{C}$  at the bottom of a 1,500-m-deep square box. For a permeability of about  $2 \times 10^{-15} \text{ m}^2$ , using seawater properties, they simulated a steady-state temperature field and an exiting fluid temperature of about  $380 \text{ }^\circ\text{C}$ . In the same paper, they also used permeabilities of about  $4 \times 10^{-15}$  and  $10^{-14} \text{ m}^2$ , for which the exiting fluid temperature varied from 350 to 450 and from 380 to  $450 \text{ }^\circ\text{C}$ , respectively. We performed similar simulations to test our numerical scheme.

Convection is simulated in an open-top box as displayed in Fig. 7. The top boundary of the domain represents a flat seafloor at a constant pressure ( $P = 240 \text{ bars}$ ). The temperature of the fluid which penetrates into the permeable medium is fixed at  $T = 2 \text{ }^\circ\text{C}$  although a zero heat diffusive flux condition is imposed for the fluid which exits from the medium. In this section, we use a Dirichlet-type condition at the bottom boundary of the domain for the temperature that we take equal to a cutoff value of  $600 \text{ }^\circ\text{C}$  [54, 73]. In the context of hydrothermal circulation, the cutoff designates the temperature at which rocks become too ductile to allow any through-flowing water. As our code is time intensive, only a coarse mesh made of 6,400 square cells is used. The surface area of the cells is equal to  $350 \text{ m}^2$ . The permeability field is assumed homogeneous and isotropic. We investigate two values

**Table 3** Parameters used in all simulations

Symbol	Physical parameter	Value	Unit
$\alpha_f$	Fluid expansivity	$-\frac{1}{\rho_f} \frac{\partial \rho_f}{\partial T}  _P$	$^\circ\text{C}^{-1}$
$\beta_f$	Fluid compressibility	$\frac{1}{\rho_f} \frac{\partial \rho_f}{\partial P}  _T$	$\text{Pa}^{-1}$
$\lambda_{\text{eff}}$	Thermal conductivity	2.0	$\text{J m}^{-1} \text{ s}^{-1} \text{ }^\circ\text{C}^{-1}$
$\mu_f$	Fluid viscosity	EOS	$\text{Pa s}$
$\rho_f$	Fluid density	EOS	$\text{kg m}^{-3}$
$\rho_r$	Rock density	2,700	$\text{kg m}^{-3}$
$c_f$	Fluid isobaric heat capacity	EOS	$\text{J kg}^{-1} \text{ }^\circ\text{C}^{-1}$
$c_r$	Rock isobaric heat capacity	880	$\text{J kg}^{-1} \text{ }^\circ\text{C}^{-1}$
$\phi$	Porosity	0.1	–
$g$	Gravitational acceleration	9.81	$\text{m s}^{-2}$
$k$	Intrinsic permeability	Variable	$\text{m}^2$

of the intrinsic permeability:  $k = 10^{-15} \text{ m}^2$  and  $k = 10^{-14} \text{ m}^2$ . The parameters of the model are given in Table 3.

Figure 8I and II displays the temperature and velocity fields obtained with a homogeneous permeability, equal to  $10^{-14}$  and  $10^{-15} \text{ m}^2$ , respectively. In both cases, as already mentioned, a constant temperature equal to  $600 \text{ }^\circ\text{C}$  is imposed at the bottom boundary of the domain. Although this temperature is lower than the  $1,000 \text{ }^\circ\text{C}$  imposed in Coumou et al. [16], we found very similar behaviors. For  $k = 10^{-14} \text{ m}^2$ , the temperature and velocity fields are unsteady (Fig. 8I). The number of main plumes varies from 3 to 4 with time. The upward flow zones are narrow, from 100 to 300 m wide, and thin near the venting surface to between 50 and 150 m wide. Maximum venting temperatures oscillate between  $335$  and  $365 \text{ }^\circ\text{C}$  with a period on the order of decades. These values are lower than the one published in Fontaine and Wilcock [24], but in agreement with Coumou et al. [16] who imposed a much higher bottom temperature, a higher entering fluid temperature ( $10 \text{ }^\circ\text{C}$  rather than  $2 \text{ }^\circ\text{C}$ ), and a lower model thickness. For  $k = 10^{-14} \text{ m}^2$ , Fontaine and Wilcock [24] argued that the difference between their results and those published in Coumou et al. [16] was probably due to the higher pressure range (300–450 bars) explored and to the seawater properties used. The strongest velocity values are obtained from the upward flow zones where they are equal on average to  $1.5 \times 10^{-7} \text{ m s}^{-1}$ . The thinning of the flow section near the exiting zone is concomitant with the rise of the velocity value to about  $4.5 \times 10^{-7} \text{ m s}^{-1}$ . In the recharge zone, values of the Peclet number are always less than 2. On the contrary, near the heat source and in the upward zone, where the fluid flow focuses, the Peclet number

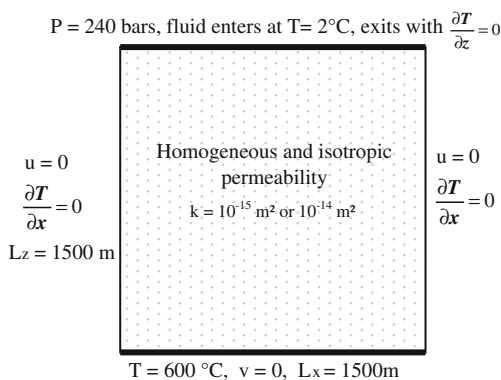


**Fig. 7** Model setup used in Section 3.2

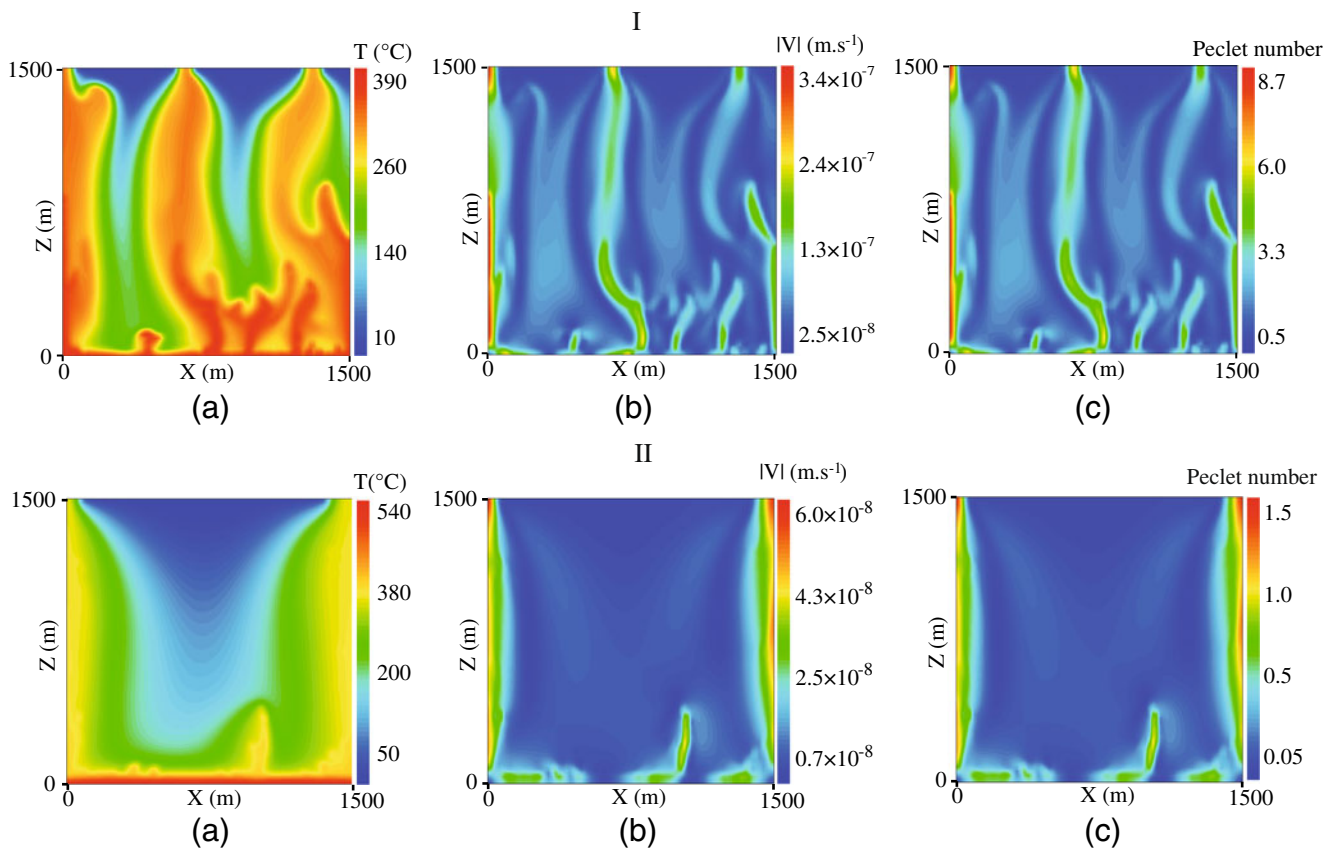


**Fig. 8** Snapshots of the fields of (a) temperature, (b) velocity, and (c) Peclet number for (I)  $k=10^{-14}$  m<sup>2</sup> and for (II)  $k=10^{-15}$  m<sup>2</sup>. A constant temperature (600 °C) is imposed at the bottom of a 1,500-m-deep square domain (Section 3.2)

becomes greater than 2, reaching a maximum value of about 9.

For  $k = 10^{-15}$  m<sup>2</sup> (Fig. 8II), although new plumes are forming in a period varying from 40 to 100 years at the middle of the bottom boundary, temperature and velocity fields are less unsteady than those obtained for  $k = 10^{-14}$  m<sup>2</sup>. Here again, the upward flow zones are narrow and get narrower similar to the venting surface. The two main plumes stay along the side boundaries. Close to the venting temperature published in Coumou et al. [16] and Fontaine and Wilcock [24], maximum venting temperatures stabilize at  $370 \pm 5$  °C and maximum velocities reach values of about  $6 \times 10^{-8}$  m s<sup>-1</sup>. As the Peclet number is always less than 1.5, the numerical scheme is everywhere second-order in space.

For a flat bottom boundary, Jupp and Schultz [40] showed that for identical pressures as those used in the present paper, plumes of pure water form at about 400 °C when a temperature greater than 500 °C is imposed at the bottom of a 1,000-m-deep domain. They also argued that isotherms higher than 400 °C are confined to the thin bottom boundary layer. This behavior also has been observed in previous papers [16].

This result is still true in the case of the H<sub>2</sub>O–NaCl system where phase separation can occur [19]. Figure 8I and II shows that in our calculations, regardless of the permeability value, the isotherm  $T = 400$  °C is also very close to the bottom boundary.

Although our model setup differs slightly from that of Coumou et al. [16] and coarse meshes are used, the results of the simulations we performed with the Cast3M code are fully consistent with their findings [16]. The fact that all the numerical simulations presented in Section 3 give results similar to those already published allows us to conclude that our numerical tool behaves satisfactorily and can be used safely for further applications.

#### 4 Application: modeling of the Rainbow vent site

##### 4.1 The Rainbow site: available data

The Rainbow vent field is located at 36°13.8'N–33°54.15'W at a depth of about 2,275–2,335 m. It is 100 m long and 200 m wide [20, 27]. Since its discov-

ery [32] and the first analyses of venting fluid samples [13], the chemistry and temperature of the vents have remained stable for more than a decade [12, 13, 20, 63]. All vented fluids exhibit a similar temperature (between 354 and 367 °C) and a similar geochemical composition, suggesting that they are probably issued from a common source [12, 63]. The Rainbow vent site has an estimated lifetime of about 23,000 years [42]. Active and dead smokers are scattered on a sulfide mound with a small surface area (about 20,000 m<sup>2</sup>) [12, 50]. This suggests that the site location has been stable for at least 20,000 years.

Furthermore, all the chlorine end-member concentrations in the Rainbow fluids are significantly greater than in local ambient seawater (4.42 to 4.69 wt% NaCl at Rainbow versus 3.2 wt% for seawater). The stability of high-Cl fluid venting at Rainbow over more than 10 years may be interpreted as the result of a deep brine layer, formed by phase separation, that is supplying salt to the circulating hydrothermal fluid. This hypothesis is in agreement with recent multiphase simulations of brine–vapor interactions at mid-ocean ridge hydrothermal systems [19]. Indeed, Coumou et al. [19] showed that venting of exclusively high-salinity fluids can only be achieved by mining a previously formed brine layer with a single-phase fluid (NB. according to Coumou et al. [19], two-phase upflow zones are likely to form only for shallow ocean depths ~1,500 m). This is in line with the conclusions of Schoofs and Hansen [62] who show that venting of fluid with salinity higher than seawater is possible when the brine layer mixes with seawater convecting above it. Charlou et al. [12] used the high chlorinity of Rainbow vents to calculate the pressure and temperature at which a brine with a similar salinity would be produced from phase separation of seawater. The fluid is then assumed to travel in the single-phase area during upflow and to be vented at the seafloor. Charlou et al. [12] estimate from  $P$ – $T$ – $x$  diagram that this high-salinity fluid can be produced by the phase separation at  $T \sim 430$  °C and  $P \sim 370$  bars. This pressure is ~140 bars greater than the seafloor pressure, thus corresponding to a depth of 1,400 m. To which extent this depth can be used to constrain the thickness of the hydrothermal system is difficult to say. Phase separation may indeed occur deeper, producing a higher salinity brine, whose salinity may subsequently decrease by diffusion/mixing during upflow. How much deeper is difficult to constrain, because it depends on the efficiency of diffusion in the upflow zone, which is largely unknown. In a recent paper, Seyfried et al. [63] emphasized this lack of knowledge of the hydrothermal characteristics of the Rainbow site and stated that the temperature and pressure of the subseafloor reaction

zone at Rainbow cannot be determined unambiguously. Hence, they arbitrarily assumed a subseafloor temperature and pressure of 400 °C and 500 bars, respectively, which allowed them to use the experimental study of Saccocia and Seyfried [61] performed at a pressure of 500 bars. In our study, we assume a 1,400-m-thick system. A sensitivity analysis is made (see Section 4.3.1) that shows that this uncertainty on the thickness of the domain has a limited impact on the results and conclusions of our study.

Based on the <sup>3</sup>He budget of the site, the estimated mass flux of hot seawater exiting at the Rainbow vent field is  $490 \pm 220 \text{ kg s}^{-1}$  [33, 38]. The active chimneys of the Rainbow vent site lay on a 200-m-long and 100-m-wide field. Hence, the estimated mass flux per square meters, denoted  $Q_s$ , verifies

$$1.35 \times 10^{-2} \text{ kg s}^{-1} \text{ m}^{-2} < Q_s < 3.55 \times 10^{-2} \text{ kg s}^{-1} \text{ m}^{-2}. \quad (20)$$

The aim of the following sections is to build 2D-model setups that can simulate the measured maximum temperatures and fluxes of the Rainbow site.

## 4.2 Initial model setup

Many different model configurations would be able to reproduce the venting characteristics observed in situ. However, we tried to constrain as much as possible the model setup from field data.

As already mentioned, the aim of our work is not to construct a precise model of the Rainbow hydrothermal site but rather to use a conceptual model of the site in order to identify the first-order physical controls of fluid convection at such black smoker systems. From chemistry and temperature data discussed in Section 4.1, we assumed that the fluid is in the single-phase regime and we used the IAPWS formulation for pure-water properties [35]. As the critical point of pure water is at  $T = 373.976$  °C and  $P = 220.6$  bars [35], the simulated pressures are always larger than the critical point, and the assumption of a single-phase fluid is justified. Such assumptions have also been done and discussed by Coumou et al. [18] to perform 3D simulations of mid-ocean ridge hydrothermal systems. Furthermore, by comparing results of advanced models such as CSMP++ [29, 30] or FISHES [45, 46] considering the systems H<sub>2</sub>O–NaCl or only pure water, simulated temperature and flux values are close in the two cases. Using the model setup of Coumou [19], Driesner [21] showed that for an imposed pressure  $P = 250$  bars at the top of their 2D model, simulation of hydrothermal circulation using pure-water or sea-

water properties exhibits similar venting temperatures. Hence, in the context of the Rainbow site, we assume that our simplifications have only minor consequences on the final results (see Sections 4.4 and 4.5).

In the case of a homogeneous permeability field and a flat bottom boundary, the 400 °C isotherm is confined to a thin (50 m deep) boundary layer, very close to the cutoff (see Section 3.2). Thus, as discussed in the previous section, the pressure  $P \sim 370$  bars and the temperature  $T \sim 430$  °C were used to estimate the depth of water circulation, giving a result of  $L_z = 1,400$  m. However, if we consider the formation of brine due to phase separation, the uncertainty on the depth value might be about 200 m [19]. Thus, as the first step, we investigated the sensitivity of the system to the domain thickness in the range 1,200–1,600 m (see Section 4.3.1).

We first took permeability values on the order of  $10^{-15}$  m<sup>2</sup>, because the Peclet number is less than 2 (see Section 3.2); thus, our numerical scheme is second order. Furthermore, in Section 3.2, we showed that our simulation for  $k = 10^{-15}$  m<sup>2</sup> was in good agreement with published results [16, 24]. For these two main reasons, we can rely on this permeability value to study the consequences of the change of the temperature boundary condition (see Figs. 7 and 9) and the consequences of the variation of the domain thickness. Nevertheless, estimated high values of mass fluxes at the Rainbow vent site require an investigation of greater permeability values [25, 45, 47, 48]. Hence, as the second step, we performed a sensitivity test for permeability with three values of  $k$ :  $k = 10^{-14}$ ,  $k = 10^{-13}$ , and  $k = 10^{-12}$  m<sup>2</sup> (see Section 4.3.2). For symmetry reasons, in all simulations, only half of the domain is simulated.

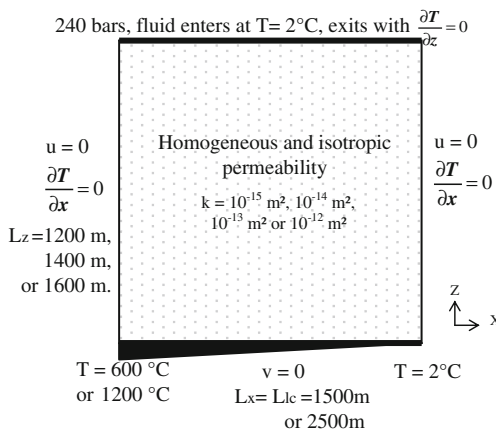


**Fig. 9** Modeling of the Rainbow site. First model setup uses  $L_x = 1,500$  m, in Sections 4.3.1 and 4.3.2, for simulations 1–6 (see Table 4). The second uses  $L_x = 2,500$  m, in Sections 4.3.3 and 4.3.4, for simulations 7–9 (see Table 4)

The geological context of slow-spreading ridges does not fit with the layered crust model that is commonly representative of fast-spreading ridge geology [52]. Furthermore, the detailed mechanisms by which hydrothermal heat transfer occurs are not well constrained. Although several previous papers described the bottom boundary of their model realistically [18, 25, 26], we assumed a single-fluid source for all smokers (see Section 4.1) and imposed a Dirichlet boundary condition at the bottom of the domain: the bottom temperature decreases linearly from  $T = T_{\max}$  from the lower left side of the domain to  $T = T_{\min}$  along a distance  $L_{lc}$  (see Fig. 9). The values of  $T_{\max}$ ,  $T_{\min}$ , and  $L_{lc}$  are strongly linked. In the first step, the temperature  $T_{\max}$  was fixed equal to the cutoff value 600 °C [54, 73]. We present a brief study of the influence of this choice of  $T_{\max}$  in Section 4.3.4.  $T_{\min}$  was fixed at 2 °C (temperature of ambient seawater). Imposing a decreasing temperature from the cutoff value to the ambient seawater value and a no-flow boundary at the bottom of the domain remains a conceptual choice. However, this is the simplest way to organize a single-plume hydrothermal circulation while restraining the numerical framework changes from the one of the validation cases. Furthermore, by doing this, cold water coming from the right side of the porous domain can horizontally displace along the bottom boundary, whereas a no-flow boundary is imposed at the right side. This allows us to observe the formation of the boundary layer and the temperature at which destabilization begins. Clearly, the no-flow condition of the bottom boundary takes a much more geological sense when we set  $T_{\max}$  to 1,200 °C (see Section 4.3.4). A preliminary study with a 3,000-m-wide domain allowed us to observe that more than 85 % of the fluid moved in the area located directly above the bottom boundary where increasing temperature was imposed. Hence, we limited the width of the domain  $L_x$  to  $L_{lc}$ .  $L_{lc}$  is equal to 1,500 m in Sections 4.3.1 and 4.3.2 (see Fig. 9) and is fixed to 2,500 m in Sections 4.3.3 and 4.3.4 (see Fig. 9). All other parameter values are the same as those already used in previous sections (see Table 2). In Sections 4.3.1 and 4.3.2, the mesh is made of 300-m<sup>2</sup> square cells. In Sections 4.3.3 and 4.3.4, the mesh is heterogeneous and made of 6,400 rectangular cells. The mesh is coarse at the top right corner where the greatest cell surface area is  $\sim 2,000$  m<sup>2</sup>. The grid fines towards the bottom and left-side boundary where the smallest surface area is 100 m<sup>2</sup>. However, the high-permeability values, such as  $k = 10^{-12}$  m<sup>2</sup>, of simulations 6 and 9 are numerically demanding to be realistically described as the system becomes purely convective. Thus, in order to investigate the consequences of the use of a coarse

**Table 4** Modeling of the Rainbow hydrothermal site

No.	$L_x$ (m)	$L_z$ (m)	$k$ ( $m^2$ )	$T_{max}$ ( $^{\circ}C$ )
1	1,500	1,200	$10^{-15}$	600
2	–	1,400	–	–
3	–	1,600	–	–
4	–	1,400	$10^{-14}$	–
5	–	–	$10^{-13}$	–
6	–	–	$10^{-12}$	–
7	2,500	–	$10^{-13}$	–
8	–	–	–	1,200
9	–	–	$10^{-12}$	–

Parameters of the model setups for nine simulations:  $L_x$  and  $L_z$  are the domain width and thickness, respectively,  $k$  is the intrinsic permeability, and  $T_{max}$  is the maximum temperature imposed at the lower left side of the domain

mesh, we also calculated simulations 6 and 9 using a very high-resolution mesh made of 16,000 and 19,200 grid elements, respectively. The surface value remains lower than  $70 m^2$  in a large zone above the bottom boundary. These surface values are much lower than the  $25 m \times 25 m$  used by Lewis and Germanovich [46], and such a grid made of  $75 m^2$  elements is considered to be a high-resolution grid in Coumou et al. [16]. We refined the grid near the base of the domain. Thus, the boundary layer is supposed to develop in a grid made of  $4\text{-}m^2$  surface elements at the bottom left corner. This surface area increases to a value of  $60 m^2$  at the bottom right corner. Along the left boundary, the surface area of the elements increases from 4 to  $100 m^2$ . This high-resolution grid is regular and made of rectangular elements. It is adapted to the numerical scheme we used and ensures its stability [44]. Characteristics of all configurations are summarized in Table 4.

Finally, we will demonstrate and discuss the fact that high exiting temperatures and high values of fluxes, such as those measured at the Rainbow site, are con-

straints leading us to develop a more complex model in Sections 4.4 and 4.5.

### 4.3 Results

All simulations presented in this section started with a constant temperature field equal to  $T_{min}$  and were pursued until the time-averaged venting temperature stabilized.

#### 4.3.1 Influence of the domain thickness

We first investigated the sensitivity of the venting temperature to the thickness of the domain. We performed three simulations with three thicknesses:  $L_z = 1,200, 1,400,$  and  $1,600 m$  (simulations 1–3 in Table 4). In all cases, the permeability of the porous medium is assumed homogeneous and equal to  $10^{-15} m^2$ . After some time, all simulations show the same global behavior: cold water enters into the domain through the top boundary facing the colder area of the bottom boundary (Fig. 10). This water travels downward, warms up near the bottom boundary layer, and finally returns to the top of the domain along the left boundary. We observed no clear influence of the thickness of the domain on the maximum fluid velocity value. In all cases, the velocity reaches its maximum value in the discharge zone, at a few hundred meters above the bottom boundary layer. This maximum value is about  $5 \times 10^{-8} m s^{-1}$ . Finally, the density increases due to the cooling of the fluid as it moves upwards to the top boundary. As a consequence, velocity decreases.

Time-averaged temperature of exiting fluid decreases slightly as thickness increases: it is equal to 355, 350, and  $346^{\circ}C$  for the 1,200-, 1,400-, and 1,600-m-thick

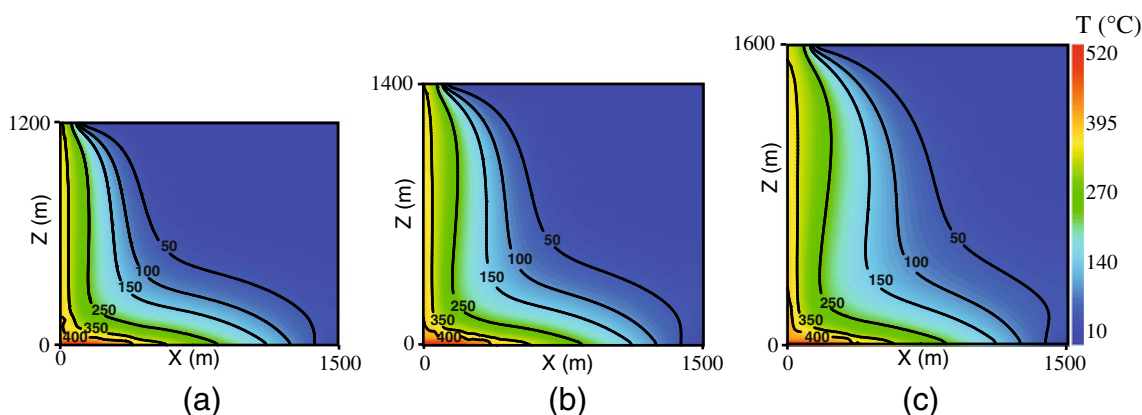


**Fig. 10** Temperature fields for three various values of the domain thickness: **a**  $L_z = 1,200 m$ , **b**  $L_z = 1,400 m$ , and **c**  $L_z = 1,600 m$ . In all three cases,  $L_x = 1,500 m$  and  $k = 10^{-15} m^2$  (Sec-

tion 4.3.1). A linearly decreasing temperature (from 600 to  $2^{\circ}C$  from the left side to the right side) is imposed at the bottom of the domain

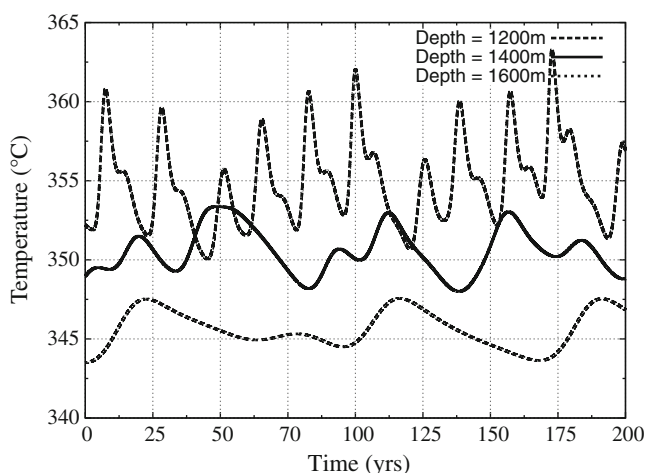


**Fig. 11** Maximum temperature of the exiting hydrothermal fluid versus time for three various values of the domain thickness:  $L_z=1,200$  m (dashed line),  $L_z=1,400$  m (solid line), and  $L_z=1,600$  m (dotted line). In all three cases,  $L_x=1,500$  m and  $k=10^{-15}$  m<sup>2</sup>. A linearly decreasing temperature (from 600 to 2 °C from the left side to the right side) is imposed at the bottom of the domain (Section 4.3.1)

domain, respectively (Fig. 11). These values are 15 to 24 °C lower than the exiting fluid temperature found when a constant bottom temperature is imposed (see Section 3.2). The maximum amplitude of oscillations also decreases as thickness increases: equal to 12, 8, and 5 °C for 1,200, 1,400, and 1,600 m, respectively. In the same way, the period of the oscillations increases: equal to about 20, 50, and 90 years for 1,200, 1,400, and 1,600 m, respectively. These observations are in agreement with the expected behavior for such a diffusive system. As depth increases, thermal-diffusion effects smooth the perturbations that growing plumes breed. Finally, we conclude that a small uncertainty on the depth domain has only a slight impact on both temperatures and fluid velocities. In the following, we will take  $L_z=1,400$  m, the depth value estimated in Charlou et al. [12] for the 430 °C isotherm.

### 4.3.2 Influence of permeability

In this section, we investigated the sensitivity of the simulated hydrothermal system to the permeability value. Three simulations were performed with three various homogeneous permeabilities:  $k=10^{-14}$  m<sup>2</sup>,  $k=10^{-13}$  m<sup>2</sup>, and  $k=10^{-12}$  m<sup>2</sup> (simulations 4–6 in Table 4). In each case, the thickness of the domain is equal to 1,400 m. Figure 12 displays the evolution versus time of the maximum temperature of exiting fluid at the top of the domain. We clearly observe that the maximum temperature decreases as permeability increases. This can be explained by two mechanisms

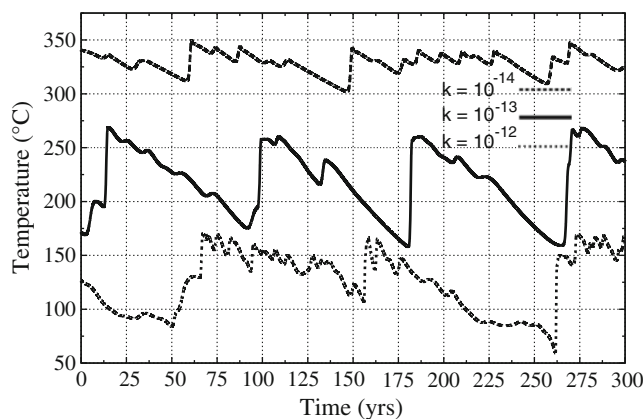


**Fig. 12** Maximum temperature of the exiting hydrothermal fluid versus time for three various values of permeability:  $k=10^{-14}$  m<sup>2</sup> (dashed line),  $k=10^{-13}$  m<sup>2</sup> (solid line), and  $k=10^{-12}$  m<sup>2</sup> (dotted line). In all three cases,  $L_x=1,500$  m and  $L_z=1,400$  m. A linearly decreasing temperature (from 600 to 2 °C from the left side to the right side) is imposed at the bottom of the domain (Section 4.3.2)

that act in synergy: as the fluid flow becomes stronger, thermal diffusion at the bottom of the domain becomes less efficient for the water to warm up (see Fig. 13). Furthermore, next to the upward flow, the supply of cold fluid, its dilution in hot fluid, and the loss of heat by diffusion/dispersion become increasingly important. Meanwhile, amplitudes of oscillations clearly increase with permeability from a few degrees for  $k=10^{-15}$  m<sup>2</sup> to a hundred of degrees for  $k=10^{-13}$  m<sup>2</sup> and for  $k=10^{-12}$  m<sup>2</sup>. Maximum fluxes per unit area (and total mass flux per meter of ridge), denoted  $Q_s$  in Section 4.1, are about  $2 \times 10^{-4}$  kg s<sup>-1</sup> m<sup>-2</sup> ( $\sim 4 \times 10^{-2}$  kg s<sup>-1</sup> m<sup>-1</sup>),  $10^{-3}$  kg s<sup>-1</sup> m<sup>-2</sup> ( $\sim 2 \times 10^{-1}$  kg s<sup>-1</sup> m<sup>-1</sup>), and  $4 \times 10^{-3}$  kg s<sup>-1</sup> m<sup>-2</sup> ( $\sim 8 \times 10^{-1}$  kg s<sup>-1</sup> m<sup>-1</sup>) for  $k=10^{-14}$  m<sup>2</sup>,  $k=10^{-13}$  m<sup>2</sup>, and  $k=10^{-12}$  m<sup>2</sup>, respectively. Regardless of the permeability value, the simulated fluxes of the exiting fluid are far lower than values inferred from geochemical data. When simulation 6 is computed using the 16,000-element grid, the bottom boundary layer is 0.5 to 2 m thick and is described by 1 to two horizontal layers of grid elements. The averaged maximum temperature is about 30 % higher than the one obtained with the coarse mesh previously used, but the maximum mass flux is similar ( $\sim 5 \times 10^{-3}$  kg s<sup>-1</sup> m<sup>-2</sup>). Even if we strongly refined the calculation grid, the overall behavior of the system is close to the one previously described, and the main conclusions are the same as previously. Mass fluxes and temperatures are much lower than those expected.

### 4.3.3 Influence of the width of the domain

We performed a simulation with a 2,500-m-wide domain. The thickness of the domain is equal to 1,400 m,

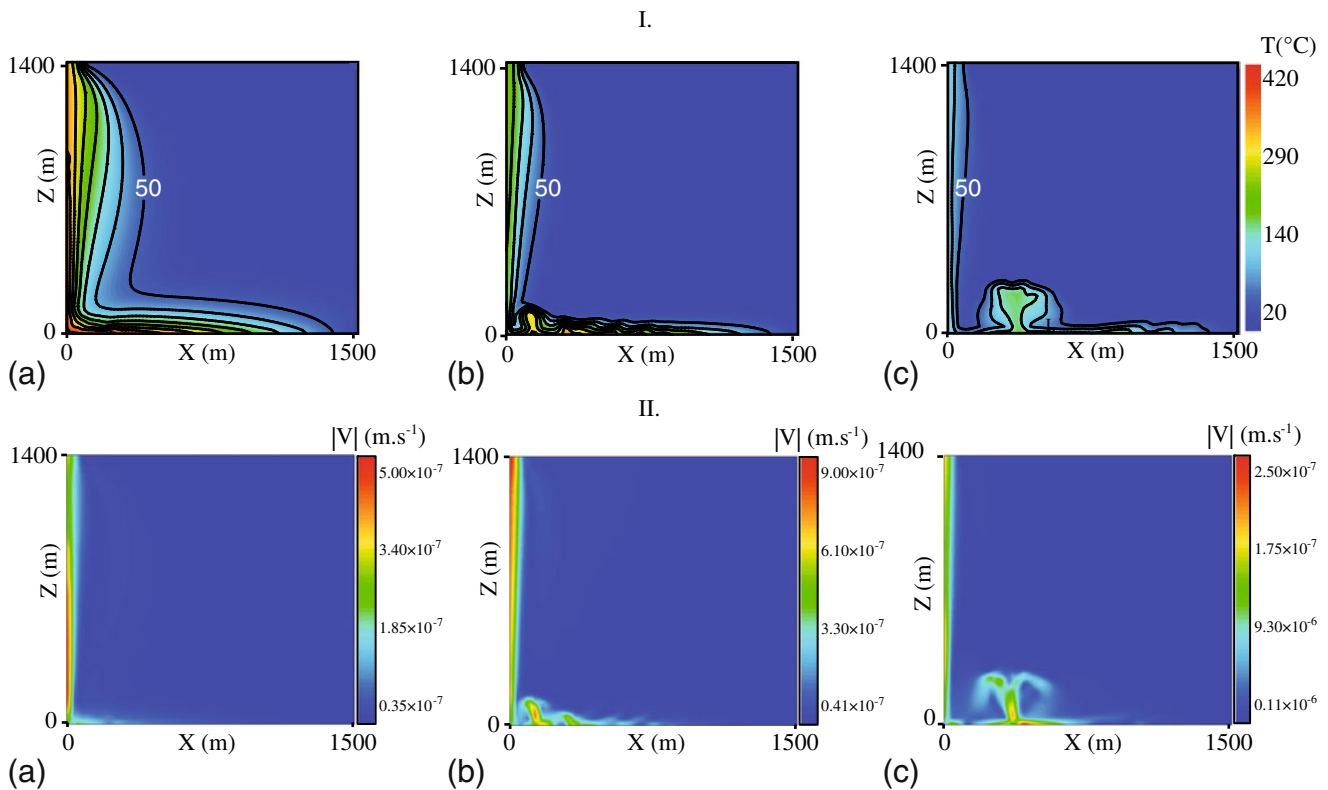


**Fig. 13** Influence of permeability on (I) the temperature field and (II) the velocity field for three various values of permeability: (a)  $k=10^{-14} \text{ m}^2$ , (b)  $k=10^{-13} \text{ m}^2$ , and (c)  $k=10^{-12} \text{ m}^2$ . In all cases,  $L_x=1,500 \text{ m}$  and  $L_z=1,400 \text{ m}$ . A linearly decreasing

temperature (from  $600$  to  $2 \text{ }^\circ\text{C}$  from the left side to the right side) is imposed at the bottom of the domain (Section 4.3.2). In group I, *solid lines* are isotherms with values increasing from  $50 \text{ }^\circ\text{C}$  by a  $50 \text{ }^\circ\text{C}$  step

as in Section 4.3.2, and  $k = 10^{-13} \text{ m}^2$  (Fig. 9, simulation 7 in Table 4). In this case, the upflow zone remains on the extreme left side of the domain. The maximum value of the exiting fluid mass flux per unit area is  $1.3 \times 10^{-3} \text{ kg s}^{-1} \text{ m}^{-2}$ . The total mass flux is about  $10^{-1} \text{ kg s}^{-1} \text{ m}^{-1}$ ; thus, for a  $200\text{-m}$ -long site, mass flux is of about  $30\text{--}40 \text{ kg s}^{-1}$ . Figure 14 displays the evolution

of the maximum temperature of exiting fluid versus time. These temperatures range from  $220$  to  $347 \text{ }^\circ\text{C}$ . Most of the peak values are about  $300 \text{ }^\circ\text{C}$ . These values are logically greater than those obtained with a  $1,500\text{-m}$ -wide domain (solid line in Fig. 12), because the heat-exchange surface area at the bottom of the domain is larger in the former case. However, here again, temperatures and fluxes remain much lower than in situ estimations.

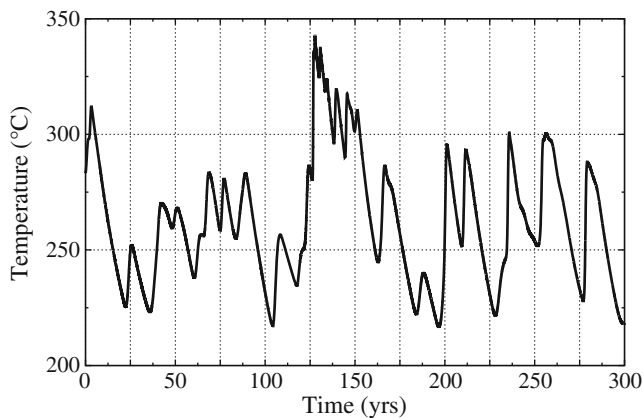


**Fig. 14** Maximum temperature of the exiting fluid versus time for  $k=10^{-13} \text{ m}^2$ ,  $T_{\text{max}} = 600 \text{ }^\circ\text{C}$  and  $L_{1c} = 2,500 \text{ m}$

#### 4.3.4 Influence of the temperature imposed at the bottom of the domain

We performed a simulation with the same characteristics as in Section 4.3.3 except for  $T_{\text{max}}$  that we fixed equal to  $1,200 \text{ }^\circ\text{C}$  which is the liquidus of basalt [65] and thus the maximum temperature at which hydrothermal fluids could eventually be exposed. We investigated the system behavior for  $k = 10^{-13} \text{ m}^2$  and  $k = 10^{-12} \text{ m}^2$  (simulations 8 and 9 in Table 4). For  $k = 10^{-13} \text{ m}^2$ , maximum temperatures of the exiting fluid oscillate between  $340$  and  $370 \text{ }^\circ\text{C}$  with a period of about  $4$  years (Fig. 15). The discharge zone is situated at the top left

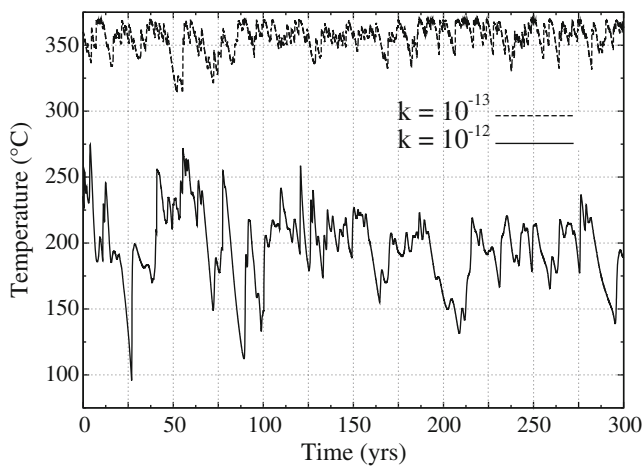


**Fig. 15** Influence of the permeability on the maximum temperature of the exiting fluid versus time for  $T_{\max} = 1,200\text{ }^{\circ}\text{C}$ ,  $L_{lc} = 2,500\text{ m}$ , and for two various values of permeability:  $k = 10^{-13}\text{ m}^2$  (dashed line) and  $k = 10^{-12}\text{ m}^2$  (solid line)

corner and is 150 m wide; however, the zone through which the hottest fluids exit is much smaller (about 40 m wide) and moves with time. Maximum mass fluxes of fluid per unit area,  $Q_s$ , are about  $3 \times 10^{-3}\text{ kg s}^{-1}\text{ m}^{-2}$ . The total mass flux is about  $2 \times 10^{-1}\text{ kg s}^{-1}\text{ m}^{-1}$ ; thus, for a 200-m-long site, mass flux is of about  $40\text{ kg s}^{-1}$ .

These are on the same orders of magnitude as in Sections 4.3.2 and 4.3.3 despite the strong increase of fluid temperature. For  $k = 10^{-12}\text{ m}^2$ , maximum temperatures are still much lower than the measured  $365\text{ }^{\circ}\text{C}$  (Fig. 15). Oscillations of great amplitude ( $>100\text{ }^{\circ}\text{C}$ ) occur, and the maximum temperatures of exiting fluid systematically vary by more than  $10\text{ }^{\circ}\text{C}$  a year. The top of the discharge zone displaces continuously along the top of the domain because of the instability of the established plume. Some plumes in formation reach the top of the domain far before the previously established plume. Thus, they enhance the latest related instability and can sometimes lead to the disappearance of the previously established plume (Fig. 16). Other simulations performed with  $L_{lc} = 3,500$  and  $4,500\text{ m}$  (not shown here) confirmed this unstable behavior. The maximum total mass flux per meter of ridge is reached for  $k = 10^{-12}\text{ m}^2$  and is equal to about  $2\text{ kg s}^{-1}\text{ m}^{-1}$ . This flux corresponds to a mass flux of  $400\text{ kg s}^{-1}$  for a 200-m-long site such as the Rainbow site and is thus on the order of magnitude of the  $490 \pm 220\text{ kg s}^{-1}$  related in Jean-Baptiste et al. [38]. However, the number of venting sites through which fluids exit is often higher than 1 and venting areas are unstable. Furthermore, the maximum mass flux value per unit area is about  $8 \times 10^{-3}\text{ kg s}^{-1}\text{ m}^{-2}$ , two times lower than the minimum

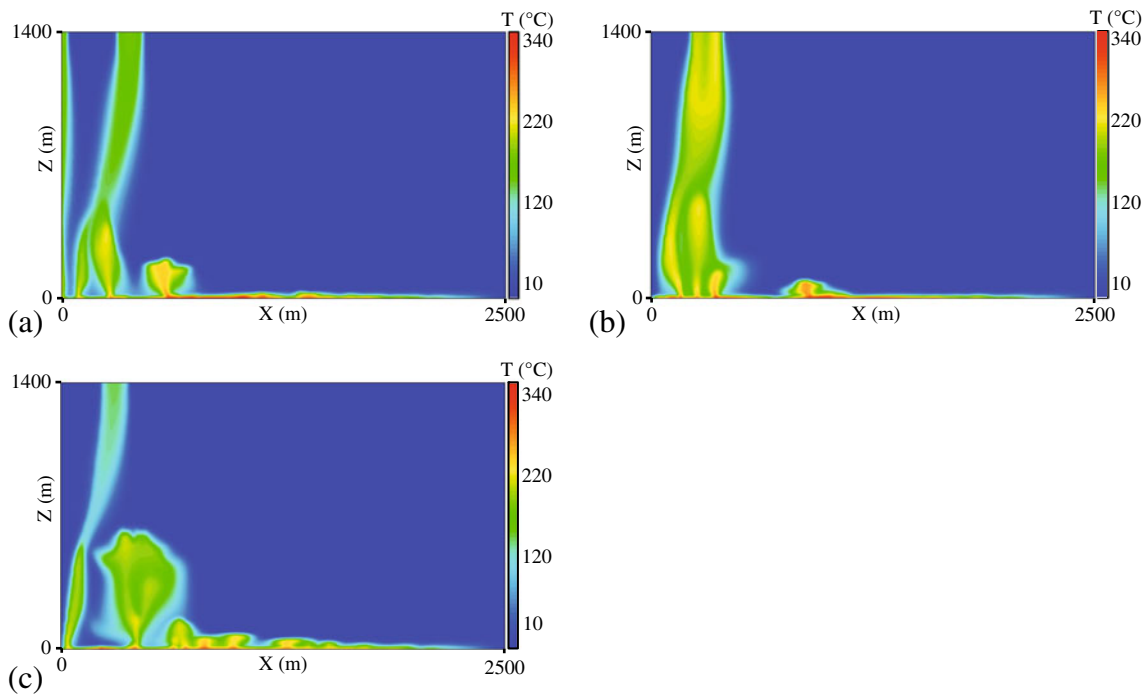
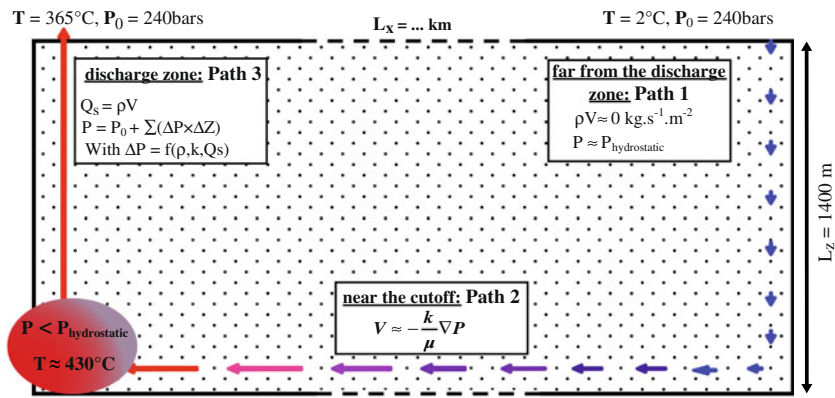


**Fig. 16** Snapshots of the temperature field for  $k = 10^{-12}\text{ m}^2$ ,  $T_{\max} = 1,200\text{ }^{\circ}\text{C}$ ,  $L_{lc} = 2,500\text{ m}$  (simulation 9 in Table 4), at **a**  $t = 560$  years, **b**  $t = 800$  years, and **c**  $t = 880$  years. The venting sites move permanently along the top boundary, and sometimes

they merge or disappear. The maximum temperature of exiting fluid oscillates between  $150$  and  $250\text{ }^{\circ}\text{C}$ , and the maximum mass flux is  $7.3 \times 10^{-3}\text{ kg s}^{-1}\text{ m}^{-2}$

**Fig. 17** Sketch of a simplified hydrothermal circulation



estimated flux for the focused flow feeding the Rainbow venting site. When the 19,200-element grid is used for simulation 9, the boundary layer is described by two horizontal layers of grid elements. The average temperature of venting fluid is about 15 % higher, and maximum exiting temperatures display similar oscillation periods and amplitudes. Venting sites fed by the largest plumes form, merge, disappear, and reappear at the top boundary. Their number oscillates between 1 and 3. Maximum mass fluxes are identical to those obtained with the coarser mesh. Thus, here again, for any type of resolution mesh, the values of mass fluxes, venting sites location and number, and temperature do not match to the site descriptions made in the literature (see Section 4.1).

4.4 Discussion: high fluxes, an evidence of the necessity of a strong permeability pathway

Regardless of the permeability value, the resolution of the mesh, the width of the domain, and the bottom imposed temperature, we never obtained a single-venting site with satisfactory mass fluxes and venting temperatures. In particular, mass fluxes are always much lower than the related estimates of the literature [33, 38]. Even in simulation 8, which exhibits high venting fluid temperatures, the maximum mass flux is four times lower than the minimum expected. Furthermore, even with very high-resolution mesh, for permeabilities greater than  $k = 10^{-15} \text{ m}^2$ , the maximum temperature of exiting fluid we simulated decreases, whereas both the amplitudes of its oscillations and mass fluxes grow. With this model setup, we never reached the in situ estimated mass flux. The decrease of the maximum temperature with the permeability increase is in good agreement with Driesner [21]. With a high-resolution mesh and a second-order accuracy scheme, Driesner [21] showed that numerical simula-

tions matched with the fluxibility approach [40]. The increase of the number of venting sites with the permeability value and the decrease of the temperature at the base of the plume we observed also seem to be in agreement with this theoretical approach [21]. However, the Dirichlet-type boundary condition we imposed for the temperature boundary condition does not allow us to make a clear quantitative comparison. Finally, it seems difficult to obtain high mass fluxes and temperatures such as those related in the literature for the Rainbow vent site by using a 2D-homogeneous porous domain. A simple analysis using Darcy’s law can confirm that we cannot obtain both high mass fluxes and high temperatures with a homogeneous permeability. In a simplified hydrothermal circulation, we can define three main zones, denoted by paths 1, 2, and 3 in Fig. 17. Paths 1, 2, and 3 correspond to the recharge zone, the bottom zone, and the discharge zone, respectively. Far from the discharge zone, in path 1 where the velocity of the entering flow is almost zero, we can assume a hydrostatic profile for the pressure field. At the bottom of the domain, along path 2, we assume that the fluid flow is horizontal. Hence, the velocity is only dependent on the pressure field. Thus, the maximum pressure at the bottom of the discharge zone at the beginning of path 3 is the hydrostatic pressure, about 390 bars in the considered case. At the same place, the maximum temperature is 430 °C and is equal to the estimated temperature of phase separation given for the Rainbow vent site [12]. In the discharge zone, which is denoted by path 3 in Fig. 17, according to our simulations, the flow is mainly upwards and the velocity field is vertical. Hence, all along path 3 where the hydrothermal flow is maximum, mass fluxes per square meter of hydrothermal water can be considered to be conservative and expressed as

$$\vec{Q}_s = \rho_f \vec{v} = -\frac{\rho_f k}{\mu_f} \left( \vec{\nabla} P + \rho_f g \vec{e}_z \right). \tag{21}$$

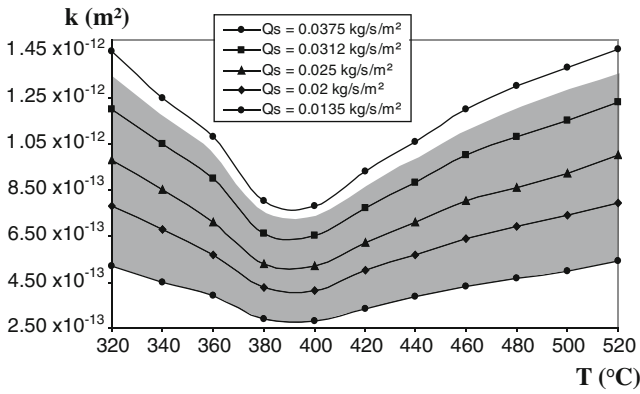


**Fig. 18** Permeability values deduced from Eqs. 21 and 22 when a constant temperature is imposed all along path 3. Curves correspond to values of the water mass fluxes: from the top to bottom, mass flux  $Q_s$  is equal to  $3.75 \times 10^{-2}$ ,  $3.125 \times 10^{-2}$ ,  $2.5 \times 10^{-2}$ ,  $2 \times 10^{-2}$ , and  $1.35 \times 10^{-2} \text{ kg s}^{-1} \text{ m}^{-2}$ , respectively. The grayed out area is the range of expected permeability values corresponding to the estimated seawater mass fluxes of the Rainbow site

Hence, the pressure gradient is given by

$$\vec{\nabla} P = -\frac{\mu_f}{\rho_f k} \vec{Q}_s - \rho_f g \vec{e}_z. \quad (22)$$

Using the IAPWS formulation for pure-water properties and several values of  $Q_s$  in the range given by Eq. 20, we calculated the pressure gradients and thus the pressure along path 3 as a function of the temperature profile and of the permeability  $k$ . The permeability  $k$  is assumed to be constant throughout the discharge zone. Then, for each temperature profile, we selected the permeability value that leads to a pressure reaching 390 bars at the bottom of the 1,400-m-deep domain. Figure 18 displays the permeability obtained from various temperature and mass flux values in path 3. It clearly shows that only a permeability of the discharge zone greater than  $2.8 \times 10^{-13} \text{ m}^2$  gives mass flux greater than the smallest estimated value ( $1.35 \times 10^{-2} \text{ kg s}^{-1} \text{ m}^{-2}$ , see Section 4.1). This permeability must be even greater than  $10^{-12} \text{ m}^2$

for the greatest estimated value of the mass flux ( $3.55 \times 10^{-2} \text{ kg s}^{-1} \text{ m}^{-2}$ , see Section 4.1). Furthermore, the use of an averaged mass flux per square meter to calculate the pressure gradient minimizes the velocity value reached in the discharge zone by homogenizing the velocity field.

As shown in Section 4.3 and its subsections, for such high permeability, in the case of a homogeneous 2D permeability field, we did not succeed in obtaining fluids of high temperature ( $>340 \text{ }^\circ\text{C}$ ) exiting at the venting site. Moreover, considering the high velocities reached in the hot fluid flow zone at such high permeabilities and the study of heat generation by serpentinization processes made by Allen and Seyfried [2], the measured temperature can probably not be reached and stabilized even if we take into account the heat production of serpentinization.

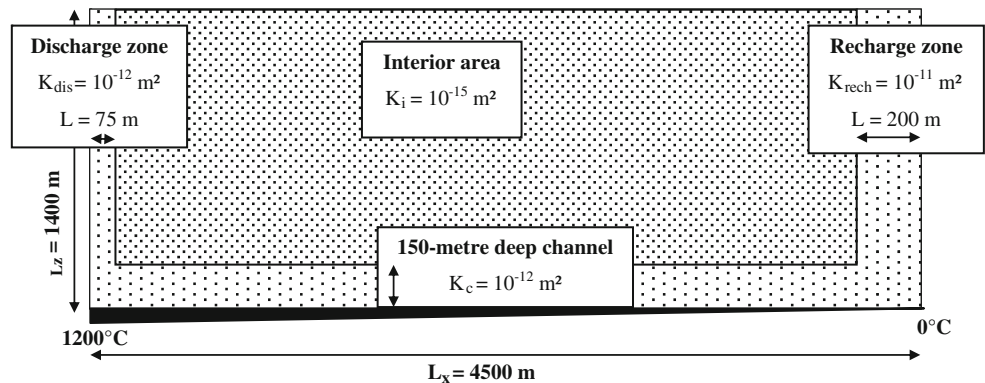
Thus, to model such a productive venting site as the Rainbow site, it is first necessary to assume the presence of a fault or a vertical preferential pathway that guides the flow of the discharge zone. Adjacent to this path, the recharge zone has to be of very low permeability ( $<10^{-15} \text{ m}^2$ ) to avoid the cooling of the upward hydrothermal plume. Mineral precipitation could eventually amplify the isolation of the plume [23, 48]. The recharge zone, near the heat source, also has to be modeled by a high-permeability path at the bottom of the domain near the heat source to sustain the exiting flow. Such a model is very close to the single-pass model studied in previous papers [45, 47, 48].

#### 4.5 A single-pass geometry to model the Rainbow vent site system

##### 4.5.1 Model geometry

The purpose of this section is not to present a sensitivity test but to validate the assumption of the existence of a permeable channel. The total thickness of the domain

**Fig. 19** Configuration of the single-pass geometry to model the Rainbow vent site



was chosen equal to 1,400 m according to the Rainbow vent field data (see Sections 4.1 and 4.3.1). The length  $L_{lc}$  is fixed equal to 4,500 m (see Fig. 19). This value is close to that estimated for the hydrothermal circulation of the Rainbow site by McCaig et al. [51]. No available data were found to constrain the surface area and permeability field of the recharge zone. Thus, above the last 200 m, along the right-side boundary, the recharge zone is schematically modeled by a 200-m-wide permeable zone. The heterogeneous permeability field is made of a low permeability zone ( $k = 10^{-15} \text{ m}^2$ ) at the center of the domain. This zone is surrounded by a high-permeability path ( $k = 10^{-12} \text{ m}^2$ ). The width of the path, equal to 75 m, is consistent with the venting surface of the Rainbow site. All along the bottom boundary, a 150-m-deep canal with a permeability  $k = 10^{-12} \text{ m}^2$  links the recharge zone (right side) to the discharge zone (left side). Increasing the 150-m thickness of this canal would increase the amplitude of maximum temperature oscillations. The mesh is made of rectangular cells with a surface area of  $400 \text{ m}^2$  at the top right corner of the domain and gradually decreasing towards the left side and bottom boundary. A minimum area of  $100 \text{ m}^2$  is reached at the left bottom boundary.

#### 4.5.2 Results

Figure 20 displays the temperature and mass flux fields when the hydrothermal circulation is established. The

**Fig. 20** Modeling of the Rainbow vent site with a single-pass geometry. Snapshots of the fields of **a** temperature and **b** mass flux  $Q_s$ , when the hydrothermal circulation is established

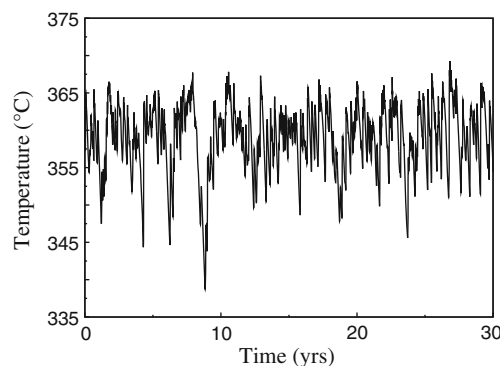
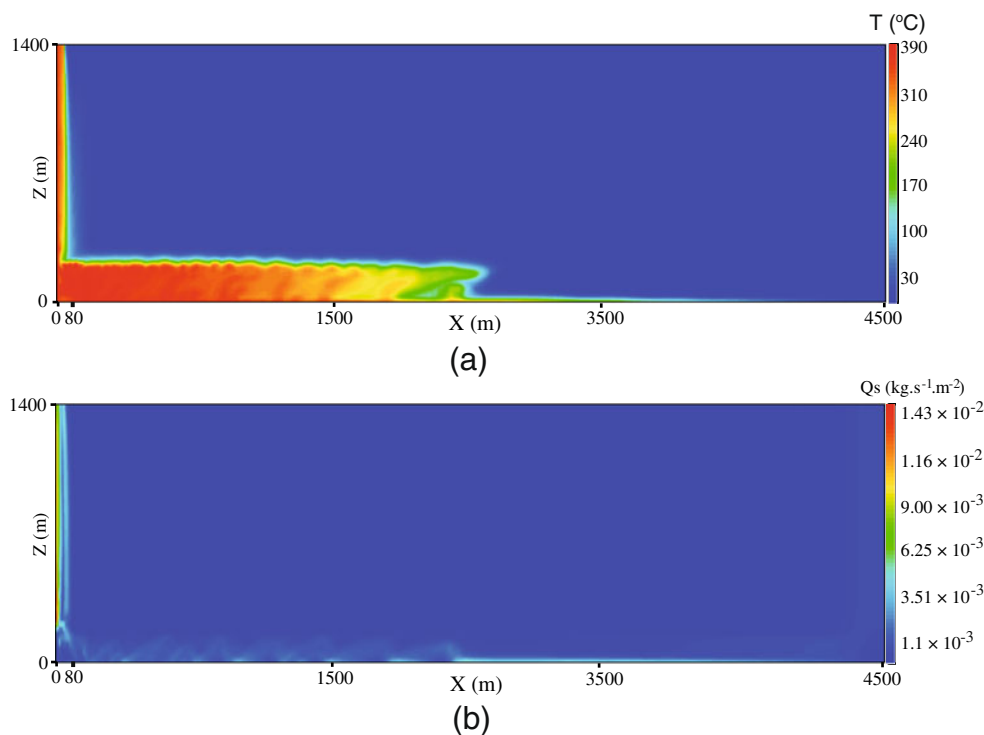


**Fig. 21** Modeling of the Rainbow vent site with a single-pass geometry. The maximum temperature of the exiting hydrothermal fluid versus time, when the hydrothermal circulation is established

upward flow remains on the left wall of the pathway and the  $350 \text{ }^\circ\text{C}$  isotherm is located about 30 to 40 m from the wall (see Fig. 20). This is in good agreement with the estimated dimensions of the Rainbow venting site, where the hottest hydrothermal fluids escape from the crust on a surface area of about  $100 \text{ m} \times 200 \text{ m}$ . Maximum temperatures of the exiting fluid reach  $360 \pm 5 \text{ }^\circ\text{C}$  (Fig. 21). At the top of the discharge zone, the mass flux values of the hydrothermal flow reach  $1.1 \times 10^{-2} \text{ kg s}^{-1} \text{ m}^{-2}$ . This value is lower than expected (at least  $1.35 \times 10^{-2} \text{ kg s}^{-1} \text{ m}^{-2}$ , see Section 4.3) but on the right order of magnitude.

## 5 Conclusion

We developed a new numerical tool in the Cast3M software framework to model hydrothermal circulation at ridge axis. We implemented two different algorithms to solve the coupled equations of fluid mass and energy balance. We employed a first-order implicit time scheme and a second-order finite-volume method for spatial discretization with the BiCGSTAB solver. The thermodynamic properties of one-phase pure water are calculated from the IAPWS formulation. This new numerical tool was validated on several test cases of convection in closed-top and open-top boxes. Simulations of hydrothermal circulation in a homogeneous-permeability porous medium also gave results in good agreement with already published simulations.

After having validated our numerical tool, we used it to construct a geometric and physical conceptual model of the Rainbow vent site. We showed that high temperatures and high mass fluxes measured at the Rainbow vent site cannot be modeled with a homogeneous-permeability porous medium. These high values require the presence of a fault or a preferential pathway right below the venting site. Hence, we constructed a single-pass model which is close to that introduced in previous papers [45, 48]. These conclusions imply that the hot reactive area of the hydrothermal circulation could be much smaller than previously expected in the case of a homogeneous-permeability porous medium. This smaller hot zone and its high water–rock ratio may have serious consequences for the current discussions about the source of hydrogen at the Rainbow vent site [12, 51, 63]. A sensitivity test will have to be made to provide a set of configurations to be used for modeling the geochemical behavior of the Rainbow vent site. Furthermore, other geometries than a 2D will have to be tested. Indeed, if we represent the Rainbow hydrothermal system as a quasi-axisymmetric system, the originally cold flow can concentrate progressively in the recharge zone as it warms up and reaches the upward flow. Thus, in this case, in the recharge zone, velocities required to support the venting flow can be less than those of the upward flow. This could increase temperatures and mass fluxes of the hydrothermal hot flow.

The final purpose of our work is to provide some keys to understanding the chemical characteristics of the fluids emitted by the active chimneys at the Rainbow vent site such as high concentrations of hydrogen. This paper will be a reference paper for future use of this code to model the geochemical behavior of the Rainbow hydrothermal field.

**Acknowledgements** Authors acknowledge Frédéric Dabbene, from the Commissariat à l’Énergie Atomique et aux Énergies Alternatives (Commissariat à l’Énergie Atomique et aux Énergies Alternatives, Gif-sur-Yvette, France) for the fruitful discussions about numerical methods. They also acknowledge Sarah Ivory for her useful language help.

## References

1. Aavatsmark, I., Barkve, T., Boe, O., Mannseth, T.: Discretization on unstructured grids for inhomogeneous, anisotropic media. Part I: derivation of the methods. *SIAM J. Sci. Comput.* **19**(5), 1700–1716 (1998)
2. Allen, D.E., Seyfried, W.E. Jr.: Serpentinization and heat generation: constraints from Lost City and Rainbow hydrothermal systems. *Geochim. Cosmochim. Acta* **68**(6), 1347–1354 (2004)
3. Baker, E.T.: Hydrothermal cooling of midocean ridge axes: do measured and modeled heat fluxes agree? *Earth Planet. Sci. Lett.* **263**, 140–150 (2007). doi:[10.1016/j.epsl.2007.09.010](https://doi.org/10.1016/j.epsl.2007.09.010)
4. Berkowitz, B., Emmanuel, S.: Suppression and stimulation of seafloor hydrothermal convection by exothermic mineral hydration. *Earth Planet. Sci. Lett.* **243**(3–4), 657–668 (2006) doi:[10.1016/j.epsl.2006.01.028](https://doi.org/10.1016/j.epsl.2006.01.028)
5. Bernard-Michel, G., Le Potier, C., Beccantini, A., Gounand, S., Chraïbi, M.: The Andra Couplex 1 test case: comparisons between finite-element, mixed hybrid finite element and finite volume element discretizations. *Comput. Geosci.* **8**(2), 187–201 (2004). doi:[10.1023/b:comg.0000035079.68284.49](https://doi.org/10.1023/b:comg.0000035079.68284.49)
6. Bischoff, J.L.: Densities of liquids and vapors in boiling NaCl–H<sub>2</sub>O solutions—A PVTX summary from 300 °C to 500 °C. *Am. J. Sci.* **291**(4), 309–338 (1991)
7. Bischoff, J.L., Rosenbauer, R.J.: An empirical-equation of state for hydrothermal seawater (3.2 percent NaCl). *Am. J. Sci.* **285**(8), 725–763 (1985)
8. Bischoff, J.L., Rosenbauer, R.J.: Liquid-vapor relations in the critical region of the system NaCl–H<sub>2</sub>O from 380 to 415 °C: a refined determination of the critical point and two-phase boundary of seawater. *Geochim. Cosmochim. Acta* **52**(8), 2121–2126 (1988)
9. Butterfield, D.A., Massoth, G.J., McDuff, R.E., Lupton, J.E., Lilley, M.D.: Geochemistry of hydrothermal fluids from Axial Seamount hydrothermal emissions study vent field, Juan de Fuca: seafloor boiling and subsequent fluid-rock interaction. *J. Geophys. Res.* **95**(B8), 12895–12921 (1990)
10. Caltagirone, J.P., Fabrie, P.: Natural Convection in a Porous Medium at High Rayleigh Numbers. I: Darcy’s Model, vol. 8. Elsevier, Issy-les-Moulineaux (1989)
11. Charlou, J.L., Donval, J.P., Fouquet, Y., Jean-Baptiste, P., Holm, N.: Geochemistry of high H<sub>2</sub> and CH<sub>4</sub> vent fluids issuing from ultramafic rocks at the Rainbow hydrothermal field (36 °14’N, MAR). *Chem. Geol.* **191**(4), 345–359 (2002)
12. Charlou, J.L., Donval, J.P., Konn, C., Ondreas, H., Fouquet, Y.: High production and fluxes of H<sub>2</sub> and CH<sub>4</sub> and evidence of abiotic hydrocarbon synthesis by serpentinization in ultramafic-hosted hydrothermal systems on the Mid-Atlantic Ridge. *AGU Geophysical Monograph Series* **188**, 265–296 (2010)
13. Charlou, J.L., Fouquet, Y., Bougault, H., Donval, J.P., Etoubeau, J., Jean-Baptiste, P., Dapigny, A., Appriou, P., Rona, P.A.: Intense CH<sub>4</sub> plumes generated by serpentinization of ultramafic rocks at the intersection of the 15

- °20'N fracture zone and the Mid-Atlantic Ridge. *Geochim. Cosmochim. Acta* **62**(13), 2323–2333 (1998)
14. Cherkaoui, A.S.M., Wilcock, W.S.D.: Characteristics of high Rayleigh number two-dimensional convection in an open-top porous layer heated from below. *J. Fluid Mech.* **394**, 241–260 (1999)
  15. Corliss, J.B., Dymond, J., Gordon, L.I., Edmond, J.M., von Herzen, R.P., Ballard, R.D., Green, K., Williams, D., Bainbridge, A., Crane, K., Andel, T.H.: Submarine thermal springs on the Galapagos Rift. *Science* **203**, 1073–1083 (1979)
  16. Coumou, D., Driesner, T., Geiger, S., Heinrich, C.A., Matthi, S.: The dynamics of mid-ocean ridge hydrothermal systems: splitting plumes and fluctuating vent temperatures. *Earth Planet. Sci. Lett.* **245**(1–2), 218–231 (2006)
  17. Coumou, D., Driesner, T., Heinrich, C.A.: The structure and dynamics of mid-ocean ridge hydrothermal systems. *Science* **321**, 1825–1828 (2008)
  18. Coumou, D., Driesner, T., Geiger, S., Paluszny, A., Heinrich, C.A.: High-resolution three-dimensional simulations of mid-ocean ridge hydrothermal systems. *J. Geophys. Res.* **114**(B7), B07104 (2009) doi:[10.1029/2008jb006121](https://doi.org/10.1029/2008jb006121)
  19. Coumou, D., Driesner, T., Weis, P., Heinrich, C.A.: Phase separation, brine formation, and salinity variation at Black Smoker hydrothermal systems. *J. Geophys. Res.* **114**(B3), B03212 (2009). doi:[10.1029/2008jb005764](https://doi.org/10.1029/2008jb005764)
  20. Douville, E., Charlou, J.L., Oelkers, E.H., Biennu, P., Jove Colon, C.F., Donval, J.P., Fouquet, Y., Prieur, D., Appriou, P.: The rainbow vent fluids (36 °14'N, MAR): the influence of ultramafic rocks and phase separation on trace metal content in Mid-Atlantic Ridge hydrothermal fluids. *Chem. Geol.* **184**(1–2), 37–48 (2002)
  21. Driesner, T.: The interplay of permeability and fluid properties as a first order control of heat transport, venting temperatures and venting salinities at mid-ocean ridge hydrothermal systems. *Geofluids* **10**, 132–141 (2010). doi:[10.1111/j.1468-8123.2009.00273.x](https://doi.org/10.1111/j.1468-8123.2009.00273.x)
  22. Emmanuel, S., Berkowitz, B.: Suppression and stimulation of seafloor hydrothermal convection by exothermic mineral hydration. *Earth Planet. Sci. Lett.* **243**(3–4), 657–668 (2006)
  23. Fontaine, F.J., Rabinowicz, M., Boulegue, J.: Permeability changes due to mineral diagenesis in fractured crust: implications for hydrothermal circulation at mid-ocean ridges. *Earth Planet. Sci. Lett.* **184**(2), 407–425 (2001)
  24. Fontaine, F.J., Wilcock, W.S.D.: Two-dimensional numerical models of open-top hydrothermal convection at high Rayleigh and Nusselt numbers: implications for mid-ocean ridge hydrothermal circulation. *Geochem. Geophys. Geosyst.* **8**(7), Q07010 (2007). doi:[10.1029/2007gc001601](https://doi.org/10.1029/2007gc001601)
  25. Fontaine, F.J., Cannat, M., Escartin, J.: Hydrothermal circulation at slow-spreading mid-ocean ridges: the role of along-axis variations in axial lithospheric thickness. *Geology* **36**(10), 759–762 (2008). doi:[10.1130/g24885a.1](https://doi.org/10.1130/g24885a.1)
  26. Fontaine, F.J., Olive, J.-A., Cannat, M., Escartin, J., Perol, T.: Hydrothermally-induced melt lens cooling and segmentation along the axis of fast- and intermediate-spreading centers. *Geophys. Res. Lett.* **38**, L14307 (2011)
  27. Fouquet, Y., Barriga, F., Charlou, J.L., Elderfield, H., German, C.R., Ondreas, H., Parson, L., Radford-Knoery, J., Relvas, J., Ribeiro, A., Schultz, A., Appriou, R., Cambon, P., Costa, I., Donval, J.P., Douville, E., Landure, J., Normand, A., Pelle, H., Poncevera, E.: FLORES diving cruise with Nautile near the Azores—first dives on the Rainbow field: hydrothermal seawater/mantle interaction. *InterRidge News* **7**(1), 24–28 (1998). Open Access version: <http://archimer.ifremer.fr/doc/00070/18133/>
  28. Foustoukos, D.I., Seyfried, W.E.: Fluid phase separation processes in submarine hydrothermal processes. *Rev. Mineral. Geochem.* **65**, 213–239 (2007)
  29. Geiger, S., Driesner, T., Heinrich, C.A., Matthai, S.K.: Multiphase thermohaline convection in the earth's crust: I. A new finite element–finite volume solution technique combined with a new equation of state for NaCl–H<sub>2</sub>O. *Transport Porous Med.* **63**(3), 399–434 (2006). doi:[10.1007/s11242-005-0108-z](https://doi.org/10.1007/s11242-005-0108-z)
  30. Geiger, S., Driesner, T., Heinrich, C.A., Matthai, S.L.: Multiphase thermohaline convection in the earth's crust: II. Benchmarking and application of a finite element–finite volume solution technique with a NaCl–H<sub>2</sub>O equation of state. *Transport Porous Med.* **63**(3), 435–461 (2006) doi:[10.1007/s11242-005-0109-y](https://doi.org/10.1007/s11242-005-0109-y)
  31. Genty, A., Le Potier, C.: Maximum and minimum principles for radionuclide transport calculations in geological radioactive waste repository: comparison between a mixed hybrid finite element method and finite volume element discretizations. *Transport Porous Med.* **88**, 65–85 (2011)
  32. German, C.R., Parson, L.M., Team, H.S., Bougault, H., Collier, D., Critchley, M., Dapoigny, A., Day, C., Eardley, D., Fearn, A., Flewellen, C., Kirk, R., Klinkhammer, G., Landure, J.Y., Ludford, E., Miranda, M., Needham, H.D., Patching, J., Pearce, R., Pelle, H., Radford-Knoery, J., Rouse, I., Scott, J., Stoffregen, P., Taylor, P., Teare, D., Wynar, J.: Hydrothermal exploration near the Azores Triple Junction: tectonic control of venting at slow-spreading ridges? *Earth Planet. Sci. Lett.* **138**(1–4), 93–104 (1996)
  33. German, C.R., Thurnherr, A.M., Knoery, J., Charlou, J.L., Jean-Baptiste, P., Edmonds, H.N.: Heat, volume and chemical fluxes from submarine venting: a synthesis of results from the Rainbow hydrothermal field, 36 °N MAR. *Deep-sea Res. Part I* **57**(4), 518–527 (2010)
  34. Graham, M.D., Steen, P.H.: *Strongly Interacting Traveling Waves and Quasiperiodic Dynamics in Porous Medium Convection*, vol. 54. Elsevier, Amsterdam (1992)
  35. Haar, L., Gallagher, J.S., Kell, G.S.: *NBS/NRC Steam Tables: Thermodynamic and Transport Properties and Computer Programs for Vapor and Liquid States of Water in SI Units*. Hemisphere Pub. Corp., Washington, DC (1984)
  36. Huyakorn, P.S., Pinder, G.F.: *Computational Methods in Subsurface Flow*, pp. 156–158. Academic, Orlando (1983)
  37. Iyer, K., Rüpke, L.H., Morgan, J.P.: Feedbacks between mantle hydration and hydrothermal convection at ocean spreading centers. *Earth Planet. Sci. Lett.* **296**(1–2), 34–44 (2010) ISSN 0012-821X. doi:[10.1016/j.epsl.2010.04.037](https://doi.org/10.1016/j.epsl.2010.04.037)
  38. Jean-Baptiste, P., Fourré, E., Charlou, J.-L., German, C.R., Radford-Knoery, J.: Helium isotopes at the Rainbow hydrothermal site (Mid-Atlantic Ridge, 36 °14'N). *Earth Planet. Sci. Lett.* **221**(1–4), 325–335 (2004)
  39. Jean-Baptiste, P., Fourré, E., Dapoigny, A., Charlou, J.L., Donval, J.P.: Deepwater mantle <sup>3</sup>He plumes over the northern Mid-Atlantic Ridge (36 °N;40°N) and the Azores Platform. *Geochem. Geophys. Geosyst.* **9**(3), Q03010 (2008). doi:[10.1029/2007gc001765](https://doi.org/10.1029/2007gc001765)
  40. Jupp, T., Schultz, A.: A thermodynamic explanation for black smoker temperatures. *Nature* **403**, 880–883 (2000)
  41. Kawada, Y., Yoshida, S., Watanabe, S.: Numerical simulations of mid-ocean ridge hydrothermal circulation including the phase separation of seawater (vol 56, pg 193, 2004). *Earth Planets Space* **56**(4), 2 (2004)
  42. Kuznetsov, V., Cherkashev, G., Lein, A., Shilov, V., Maksimov, F., Arslanov, Kh., Stepanova, T., Baranova, N., Chernov, S., Tarasenko D.: <sup>230</sup>Th/U dating of massive sulfides from the logatchev and rainbow hydrothermal fields

- (Mid-Atlantic Ridge). *Geochronometria*, vol. 25, pp 51–55 (2006)
43. Lehmann, F., Ackerer, P.: Comparison of iterative methods for improved solutions of the fluid flow equation in partially saturated porous media. *Transport Porous Med.* **31**(3), 275–292 (1998)
  44. Le Potier, C.: Finite volume scheme in two or three dimensions for a diffusion-convection equation applied to porous media with CASTEM2000. *Dev. Water Sci.* **55**(2), 1015–1026 (2004)
  45. Lewis, K.C., Lowell, R.P.: Numerical modeling of two-phase flow in the NaCl–H<sub>2</sub>O system: 2. Examples. *J. Geophys. Res.* **114**(B8), B08204 (2009). doi:[10.1029/2008jb006030](https://doi.org/10.1029/2008jb006030)
  46. Lewis, K.C., Lowell, R.P.: Numerical modeling of two-phase flow in the NaCl–H<sub>2</sub>O system: Introduction of a numerical method and benchmarking. *J. Geophys. Res.* **114**(B5), B05202 (2009). doi:[10.1029/2008jb006029](https://doi.org/10.1029/2008jb006029)
  47. Lowell, R.P., Germanovich, L.N.: *Hydrothermal Processes at Mid-Ocean Ridges: Results from Scale Analysis and Single-pass Models*. American Geophysical Union, Washington, DC (2004)
  48. Lowell, R.P., Gosnell, S., Yang, Y.: Numerical simulations of single-pass hydrothermal convection at mid-ocean ridges: effects of the extrusive layer and temperature-dependent permeability. *Geochem. Geophys. Geosyst.* **8**(10), Q10011 (2007). doi:[10.1029/2007gc001653](https://doi.org/10.1029/2007gc001653)
  49. Marcaillou, C.: *Serpentinisation et production d'hydrogène en contexte de dorsale lente: approche expérimentale et numérique*. Sciences de la Terre, de l'Univers, et de l'Environnement, Université de Grenoble (2011)
  50. Marques, A., Barriga, F., Chavagnac, V., and Fouquet, Y.: Mineralogy, geochemistry, and Nd isotope composition of the Rainbow hydrothermal field, Mid-Atlantic Ridge. *Miner. Depos.* **41**, 52–67 (2006)
  51. McCaig, A.M., Cliff, R.A., Escartin, J., Fallick, A.E., MacLeod, C.J.: Oceanic detachment faults focus very large volumes of black smoker fluids. *Geology* **35**(10), 935–938 (2007). doi:[10.1130/g23657a.1](https://doi.org/10.1130/g23657a.1)
  52. Mével, C.: Serpentinization of abyssal peridotites at mid-ocean ridges. *C. R. Geosci.* **335**, 825–852 (2003)
  53. Millard, A.: Short description of CASTEM 2000 and TRIO-EF. In: Stephansson O., Jing L., Tsang C.-F. (eds.) *Coupled Thermo-hydro-mechanical Processes of Fractured Media*, pp. 559–564. Elsevier, Rotterdam (1996)
  54. Morton, J.L., Sleep, N.H.: A mid-ocean ridge thermal model: constraints on the volume of axial hydrothermal heat flux. *J. Geophys. Res.* **90**(B13), 11345–11353 (1985). doi:[10.1029/JB090iB13p11345](https://doi.org/10.1029/JB090iB13p11345)
  55. Paniconi, C., Putti, M.: A comparison of Picard and Newton iteration in the numerical solution of multidimensional variably saturated flow problems. *Water Resour. Res.* **30**(12), 3357–3374 (1994)
  56. Potter, R.W., II, and Brown, D.L.: The volumetric properties of aqueous sodium chloride solutions from 0 ° to 500 °C at pressures up to 2000 bars based on a regression of available data in literature, U. S. Geol. Surv. Bull., 1421-C, pp. 36. (1977)
  57. Rabinowicz, M., Boulègue, J., Genthon, P.: Two- and three-dimensional modeling of hydrothermal convection in the sedimented Middle Valley segment, Juan de Fuca Ridge. *J. Geophys. Res.* **103**, 24045–24065 (1998)
  58. Rabinowicz, M., Sempéré, J.-C., Genthon, P.: Thermal convection in a vertical permeable slot: implications for hydrothermal circulation along mid-ocean ridges. *J. Geophys. Res.* **104**, 29275–29292 (1999)
  59. Rona, P.A., et al.: Black smokers, massive sulphides and vent biota at the Mid-Atlantic Ridge. *Nature* **321**, 33–37 (1986)
  60. Rudge, J.F., Kelemen, P.B., Spiegelman, M.: A simple model of reaction-induced cracking applied to serpentinization and carbonation of peridotite. *Earth Planet. Sci. Lett.* **291**(1–4), 215–227 (2010)
  61. Saccoccia, P.J., Seyfried, W.E. Jr.: The solubility of chlorite solid solutions in 3.2 wt % NaCl fluids from 300–400 °C, 500 bars. *Geochim. Cosmochim. Acta* **58**(2), 567–585 (1994)
  62. Schoofs, S., Hansen, U.: Depletion of a brine layer at the base of ridge-crest hydrothermal systems. *Earth Planet. Sci. Lett.* **180**(3–4), 341–353 (2000)
  63. Seyfried Jr, W.E., Pester, N.J., Ding, K., Rough, M.: Vent fluid chemistry of the Rainbow hydrothermal system (36 °N, MAR): Phase equilibria and in situ pH controls on seafloor alteration processes. *Geochim. Cosmochim. Acta* **75**(6), 1574–1593 (2011)
  64. Singh, S.C., Crawford, W.C., Carton, H., Seher, T., Combier, V., Cannat, M., Pablo Canales, J., Dusunur, D., Escartin, J., Miguel Miranda, J.: Discovery of a magma chamber and faults beneath a Mid-Atlantic Ridge hydrothermal field. *Nature* **442**(7106), 1029–1032 (2006)
  65. Sinton, J.M., Detrick, R.S.: Mid-ocean ridge magma chambers. *J. Geophys. Res.* **97**(B1), 197–216 (1992). doi:[10.1029/91jb02508](https://doi.org/10.1029/91jb02508)
  66. Spiess, F.N., et al.: East Pacific Rise: hot springs and geophysical experiments. *Science* **207**, 1421–1433 (1980)
  67. Straus, J.M., Schubert, G.: Thermal convection of water in a porous medium: effects of temperature and pressure-dependent thermodynamic and transport properties. *J. Geophys. Res.* **82**, 325–333 (1977)
  68. Sun, H., Feistel, R., Koch, M., Markoe, A.: New equations for density, entropy, heat capacity, and potential temperature of a saline thermal fluid. *Deep-Sea Res. Part I* **55**(10), 1304–1310 (2008)
  69. Travis, B.J., Janecky, D.R., Rosenberg, N.D.: Three-dimensional simulation of hydrothermal circulation at mid-ocean ridges. *Geophys. Res. Lett.* **18**, 1441–1444 (1991)
  70. Van der Vorst, H.: Bi-CGSTAB: a fast and smoothly converging variant of BI-CG for the solution of nonsymmetric linear systems. *SIAM J. Sci. Statist. Comput.* **13**, 631–644 (1992)
  71. Von Damm, K.L., Lilley, M.D., Shanks III, W.C., et al.: Extraordinary phase separation and segregation in vent fluids from the southern East Pacific Rise. *Earth Planet. Sci. Lett.* **206**, 365–378 (2003)
  72. Wilcock, W.S.D.: Cellular convection models of mid-ocean ridge hydrothermal circulation and the temperatures of black smoker fluids. *J. Geophys. Res.* **103**(B2), 2585–2596 (1998). doi:[10.1029/97jb03252](https://doi.org/10.1029/97jb03252)
  73. Wilson, D.S., Clague, D.A., Sleep, N.H., Morton, J.L.: Implications of magma convection for the size and temperature of magma chambers at fast spreading ridges. *J. Geophys. Res.* **93**(B10), 11974–11984 (1988). doi:[10.1029/JB093iB10p11974](https://doi.org/10.1029/JB093iB10p11974)